# A wind-blown bubble in the Central Molecular Zone cloud G0.253+0.016

Jonathan D. Henshaw [1]★ Mark R. Krumholz [1,2,3,4] Natalie O. Butterfield,[5] Jonathan Mackey [6,7] Adam Ginsburg,[8] Thomas J. Haworth,[9] Francisco Nogueras-Lara [1] Ashley T. Barnes [10] Steven N. Longmore,[11] John Bally,[12] J. M. Diederik Kruijssen [13] Elisabeth A. C. Mills,[14] Henrik Beuther,[1] Daniel L. Walker,[15] Cara Battersby,[15] Alyssa Bulatek,[8] Thomas Henning,[1] Juergen Ott[16,17] and Juan D. Soler[1]

[1] *Max Planck Institute for Astronomy, Königstuhl 17, D-69117 Heidelberg, Germany*
[2] *Research School of Astronomy and Astrophysics, Australian National University, Canberra, ACT 2611, Australia*
[3] *ARC Centre of Excellence for Astronomy in Three Dimensions (ASTRO-3D), Canberra, ACT 2611, Australia*
[4] *Institut fur Theoretische Astrophysik, Zentrum für Astronomie, Universität Heidelberg, D-69120 Heidelberg, Germany*
[5] *Department of Physics, Villanova University, 800 E. Lancaster Ave., Villanova, PA 19085, USA*
[6] *Dublin Institute for Advanced Studies, Astronomy & Astrophysics Section, 31 Fitzwilliam Place, Dublin 2, Ireland*
[7] *Dublin Institute for Advanced Studies, Centre for AstroParticle Physics and Astrophysics (CAPPA), DIAS Dunsink Observatory, Dunsink Lane, Dublin 15, Ireland*
[8] *Department of Astronomy, University of Florida, 211 Bryant Space Sciences Center, Gainesville, 32611 FL, USA*
[9] *Astronomy Unit, School of Physics and Astronomy, Queen Mary University of London, London E1 4NS, UK*
[10] *Argelander Institute für Astronomy, University of Bonn, Auf dem Hügel 71, D-53121 Bonn, Germany*
[11] *Astrophysics Research Institute, Liverpool John Moores University, IC2, 146 Brownlow Hill, Liverpool L3 5RF, UK*
[12] *CASA, University of Colorado, 389-UCB, Boulder, CO 80309, USA*
[13] *Astronomisches Rechen-Institut, Zentrum für Astronomie der Universität Heidelberg, Mönchhofstraße 12-14, D-69120 Heidelberg, Germany*
[14] *Department of Physics and Astronomy, University of Kansas, 1251 Wescoe Hall Drive, Lawrence, KS 66045, USA*
[15] *Department of Physics, University of Connecticut, 196A Auditorium Road, Unit 3046, Storrs, CT 06269, USA*
[16] *National Radio Astronomy Observatory, 1003 Lopezville Road, Socorro, NM 87801, USA*
[17] *New Mexico Institute of Mining and Technology, 801 Leroy Place, Socorro, NM 87801, USA*

## ABSTRACT

G0.253+0.016, commonly referred to as 'the Brick' and located within the Central Molecular Zone, is one of the densest ($\approx 10^{3-4}\,\mathrm{cm}^{-3}$) molecular clouds in the Galaxy to lack signatures of widespread star formation. We set out to constrain the origins of an arc-shaped molecular line emission feature located within the cloud. We determine that the arc, centred on $\{l_0, b_0\} = \{0°248, 0°018\}$, has a radius of 1.3 pc and kinematics indicative of the presence of a shell expanding at $5.2^{+2.7}_{-1.9}\,\mathrm{km\,s^{-1}}$. Extended radio continuum emission fills the arc cavity and recombination line emission peaks at a similar velocity to the arc, implying that the molecular gas and ionized gas are physically related. The inferred Lyman continuum photon rate is $N_{\mathrm{LyC}} = 10^{46.0}$–$10^{47.9}$ photons s$^{-1}$, consistent with a star of spectral type B1-O8.5, corresponding to a mass of $\approx 12$–$20\,\mathrm{M_\odot}$. We explore two scenarios for the origin of the arc: (i) a partial shell swept up by the wind of an interloper high-mass star and (ii) a partial shell swept up by stellar feedback resulting from *in situ* star formation. We favour the latter scenario, finding reasonable (factor of a few) agreement between its morphology, dynamics, and energetics and those predicted for an expanding bubble driven by the wind from a high-mass star. The immediate implication is that G0.253+0.016 may not be as quiescent as is commonly accepted. We speculate that the cloud may have produced a $\lesssim 10^3\,\mathrm{M_\odot}$ star cluster $\gtrsim 0.4\,\mathrm{Myr}$ ago, and demonstrate that the high-extinction and stellar crowding observed towards G0.253+0.016 may help to obscure such a star cluster from detection.

**Key words:** ISM: bubbles – ISM: clouds – H II regions – ISM: kinematics and dynamics – ISM: structure – Galaxy: centre.

## 1 INTRODUCTION

The Central Molecular Zone (hereafter, CMZ), i.e. the inner few hundred parsecs of the Milky Way, hosts some of the Galaxy's densest molecular clouds (Lis & Carlstrom 1994; Bally et al. 2010; Longmore et al. 2012, 2013b; Walker et al. 2015; Mills et al. 2018) and star clusters (known as the Arches and Quintuplet; Figer et al. 1999; Portegies Zwart, McMillan & Gieles 2010; Longmore et al. 2014). Of the former, G0.253+0.016 (often referred to as 'the Brick') is probably one of the most enigmatic molecular clouds in the Galaxy. Much of the interest in this cloud stems from the fact that it exhibits little evidence of widespread star formation activity (Lis et al. 1994; Immer et al. 2012; Mills et al. 2015), in spite of its high mass

★ E-mail: jonathan.d.henshaw@gmail.com

($\approx 10^5$ M$_\odot$) and mean density ($\approx 10^{3-4}$ cm$^{-3}$; Lis & Carlstrom 1994; Lis & Menten 1998; Longmore et al. 2012; Rathborne et al. 2014b; Mills et al. 2018).

Until recently, the only direct evidence for star formation within G0.253+0.016 was a single water maser (see also Lis et al. 1994; Lu et al. 2019b). This evidence has been strengthened considerably by recent high angular resolution Atacama Large Millimeter/submillimeter Array (ALMA) observations of the maser source, which reveal a small cluster of low-to-intermediate mass protostars, 50 per cent of which are driving bipolar outflows (Walker et al. 2021). Deep radio continuum observations and additional searches for maser emission have not revealed any further star formation activity (Immer et al. 2012; Rodríguez & Zapata 2013; Mills et al. 2015; Lu et al. 2019a), and all other evidence for star formation comes from indirect energy balance arguments. Lis et al. (2001) model the far-infrared/submillimetre spectral energy distribution of G0.253+0.016, and infer that the cloud's luminosity is conceivably generated by four B0 zero-age main-sequence stars. Marsh et al. (2016) report evidence of heated dust emission that follows a tadpole-shaped ridge, which they suggest may result from a chain of embedded protostars.

Clouds with the physical characteristics of G0.253+0.016, but which are not already prodigiously forming stars, do not exist within the Milky Way disc (Ginsburg et al. 2012; Urquhart et al. 2018). Consequently, G0.253+0.016 presents a unique opportunity to study the early phases of high-mass star and cluster formation under the extreme conditions found in the Galactic Centre (Longmore et al. 2012, 2013b; Rathborne et al. 2014a). Recent observational work has set out to categorize G0.253+0.016's internal structure and dynamics in order to better understand its star formation potential. The internal structure of the cloud is complex (Kauffmann, Pillai & Zhang 2013; Henshaw et al. 2019). Dust continuum and molecular line observations reveal significant substructure, with a few dozen compact cores and filaments detected in both emission and absorption (Bally et al. 2014; Johnston et al. 2014; Rathborne et al. 2014b, 2015; Federrath et al. 2016; Battersby et al. 2020; Hatchfield et al. 2020). Gas motions measured on $\sim 0.1$ pc scales are highly supersonic (Henshaw et al. 2019, 2020), resulting in widespread shocked gas emission (Kauffmann et al. 2013; Johnston et al. 2014).

Federrath et al. (2016) inferred that the internal turbulence in G0.253+0.016 is dominated by solenoidal motion, likely resulting from the strong shear induced by its eccentric orbit around the Galactic Centre (Kruijssen et al. 2019). The shear resulting from the background gravitational potential and the cloud's orbital motion may help to explain its morphology (Kruijssen et al. 2019; Petkova et al. 2021). The combination of solenoidal gas motion, a strong magnetic field (Pillai et al. 2015), and an elevated critical density threshold for star formation (Kruijssen et al. 2014; Rathborne et al. 2014b; Ginsburg et al. 2018) may explain the overall low star formation rate of G0.253+0.016.

However, there is a complication to this simple picture, in the form of an arcuate, shell-like structure detected within the cloud's interior. It has been detected in a variety of molecular species including SO (Higuchi et al. 2014), NH$_3$ (Mills et al. 2015), HNCO (Henshaw et al. 2019), and SiO (Walker et al. 2021). Both the gas and dust temperature along the rim of the arc appear to be elevated, evidenced by its clear detection in higher excitation lines of NH$_3$ [Mills et al. 2015 report detections in the (6,6) and (7,7) inversion transitions]. The arc is also co-spatial with the spine of warm dust identified by Marsh et al. (2016). Class I Methanol masers, believed to be tracing shocked gas emission that is not directly related to star formation (unlike Class II masers), are furthermore detected in a crescent-

like arrangement following the arc emission observed in NH$_3$ (Mills et al. 2015). Following detailed investigation of the dynamics of G0.253+0.016, Henshaw et al. (2019) demonstrated that the arc is coherent in both projected space and in velocity. The bulk of the emission associated with G0.253+0.016 is spread over a velocity range of $\sim 40$ km s$^{-1}$. In position–position–velocity space, there are at least two cloud components. The 'main' component is that which closely resembles G0.253+0.016 as it appears in dust continuum emission, and has a mean velocity of $\sim 37$ km s$^{-1}$. The mean velocity of the component associated with the arc is $\sim 17$ km s$^{-1}$. However, the velocity gradient associated with this latter component is such that this and the main component appear to meet (in position–position–velocity space) towards the south of the cloud (Henshaw et al. 2019).

The origin of the arc is unclear. Higuchi et al. (2014) speculate that the arc may have been generated following a collision between two molecular clouds based on the arc's morphological similarity to the structure generated in numerical simulations of cloud–cloud collisions (e.g. Habe & Ohta 1992; Takahira, Tasker & Habe 2014; Haworth et al. 2015). An alternative hypothesis, however, is that the arc is generated by stellar feedback. If confirmed, this could indicate that G0.253+0.016 is perhaps more active in its star formation than previously thought. In this work, we build on the analysis of Henshaw et al. (2019), and introduce new observations from the Karl Jansky Very Large Array (VLA),[1] to help test this hypothesis, finding that the morphology, dynamics, and energetics of the arc are all consistent to within a factor of a few of those predicted for a simple analytical model of an expanding bubble driven by the wind from a high-mass star. The paper is organized as follows. In Section 2, we describe the data used in this work, both from Henshaw et al. (2019) and our VLA observations. In Section 3, we outline our main results. Finally, in Sections 4 and 5 we discuss our findings and outline our conclusions, respectively.

## 2 DATA

### 2.1 ALMA data and SCOUSEPY decomposition

This paper makes use of the ALMA Early Science Cycle 0 Band 3 observations of G0.253+0.016 originally presented in Rathborne et al. (2014b, 2015). We summarize the observations here but refer the reader to the aforementioned papers for a more extensive description. The ALMA 12 m observations cover the full 3 arcmin × 1 arcmin extent of the cloud using a 13-point mosaic. Here, we use emission from the $4(0, 4) - 3(0, 3)$ transition of HNCO, which has proved fruitful to study the internal structure and dynamics of the cloud (Rathborne et al. 2015; Federrath et al. 2016; Henshaw et al. 2019). Rathborne et al. (2015) combine these data with single dish observations from the Millimetre Astronomy Legacy Team 90 GHz Survey (MALT90; Foster et al. 2011; Jackson et al. 2013) obtained with the Mopra 22 m telescope to recover the extended emission filtered out by the interferometer. The spatial and spectral resolution are 1.7 arcsec and 3.4 km s$^{-1}$, respectively. Throughout this paper, we adopt a distance to the Galactic Centre of $8.178 \pm 0.013$ kpc (Gravity Collaboration 2019) and assume that G0.253 + 0.016 is located at this distance (Nogueras-Lara et al. 2021a). The corresponding physical

---

[1]The VLA radio telescope is operated by the National Radio Astronomy Observatory (NRAO). The National Radio Astronomy Observatory is a facility of the National Science Foundation operated under cooperative agreement by Associated Universities, Inc.

resolution of these data is therefore ≈0.07 pc. The rms noise per 3.4 km s$^{-1}$ resolution element is 0.8 mJy beam$^{-1}$.

Henshaw et al. (2019) further process these data with the SCOUSEPY and ACORNS algorithms (Agglomerative Clustering for ORganising Nested Structures; Henshaw et al. 2016a, 2019, respectively), and again we summarize the procedure here, referring readers to the original paper for details. First, we use SCOUSEPY to decompose the spectral line emission into a set of discrete Gaussian components; we fit a total of ∼450 000 Gaussian components to ∼130 000 spectra (see fig. 2 of Henshaw et al. 2019). We next use ACORNS to cluster the Gaussian emission features identified by SCOUSEPY into hierarchical velocity-coherent regions. Out of the forest of clusters that ACORNS identifies, four of them dominate the emission profile of G0.253+0.016 (as it appears in HNCO emission), accounting for >50 per cent of the detected Gaussian components. Of these four clusters, or trees as they are referred to in Henshaw et al. (2019) (owing to the dendrogram nomenclature), two account for the overall physical appearance of G0.253+0.016. The emission associated with the first, the 'main' component, is qualitatively most similar in appearance to G0.253+0.016 as it appears in dust continuum emission (Henshaw et al. 2019, see their section 4.2). The emission profile of the second component is clearly associated with the arc focused on here, which previously had been detected in other works in different molecular species (Higuchi et al. 2014; Mills et al. 2015). This finding therefore served as the first evidence that the arc was coherent both in (projected) space and in velocity. In this work, we make use of the data products output from SCOUSEPY and ACORNS related to this latter cloud component to investigate the origins of the arc. In the remainder of the paper, we refer to the component identified by ACORNS as the parent subcloud of the arc.

## 2.2 VLA data

The VLA observations presented in this paper were taken in *C* band (4–8 GHz) with the C array configuration (5 arcsec resolution). The observations were taken in four separate observing runs, in 2017 June, with a cadence of ∼2 d between observations. The observations targeted six separate fields, 2 h on source per field. The observations used J1331+3030 (3C 286) as the bandpass calibrator and J1820−2528 as the phase calibrator. The phase calibrator was observed every 35 min during the observations. The observations were also set up to observe the full stokes parameters and therefore we used J1407+2827 as the polarization leakage calibrator. The observations were processed using the Common Astronomy Software Application (CASA)[2] pipeline, provided by NRAO, to calibrate the data. The continuum data combines the 4–8 GHz frequency coverage (3.8 GHz total bandwidth) of the *C*-band observations. The continuum data used all four observing runs which were combined in the imaging stage of the data reduction. The observations were cleaned using the CASA task tclean. The image was cleaned non-interactively down to a threshold of 0.01 mJy. We used Briggs weighting of 0.5 to improve the sensitivity and resolution of the image. The data were cleaned using the 'multiscale, multifrequency synthesis' (deconvolver='mtmfs', specmode = 'mfs') with scales of 0, 4, and 16 pixels to account for the large-scale structures present in the field. The synthesized beam size is 6″.4 × 2″.9 with a position angle −2°.5. The rms noise (estimated from emission-free regions) is 0.15 mJy beam$^{-1}$.

The radio recombination line (RRL) data presented in this paper combined the H114α, H113α, H110α, H109α, H101α, H100α, and H99α transitions. The radio continuum was subtracted in the uv-plane, using the CASA task uvcontsub, before any imaging was done. Each radio recombination transition was cleaned individually using the CASA task tclean by combining the four observing runs during the imaging process. All recombination line transitions were imaged using the same tclean parameters: 1 km s$^{-1}$ spectral resolution, 6″ × 12″ restoring beam size, velocity range of −40 to 99 km s$^{-1}$. The images were cleaned non-interactively using a set noise threshold level of 1 mJy and natural weighting to obtain the best sensitivity possible. The cleaned images were then averaged together using the CASA task immath to improve the signal-to-noise ratio in the image.

## 3 RESULTS

### 3.1 Morphology and kinematics

We present a map of the arc in the left-hand panel of Fig. 1. The colour scale in this image refers to the peak amplitude of emission features extracted using SCOUSEPY (Section 2.1) from the HNCO data (Henshaw et al. 2019). The arc can be clearly identified in this map as the ridge of emission towards the centre of the cloud (highlighted by the thick black contour).

We highlight several features of interest in the map. First, the yellow circle denotes the position of the $H_2O$ maser identified by Lis et al. (1994, see also Lu et al. 2019b), which remains the only confirmed site of embedded star formation within G0.253+0.016 (see also Walker et al. 2021). The red diamonds are the locations of H II regions and H II region candidates in close projected proximity to G0.253+0.016 (Rodríguez & Zapata 2013, though note that Mills et al. 2015 argue that the sources within the cloud are spatially filtered peaks of more extended emission, as is also seen in the 5 GHz data presented here).

Mills et al. (2015) found a number of class I $CH_3OH$ masers and maser candidates located throughout G0.253+0.016. Rather than tracing the locations of ongoing star formation, these most likely trace regions of shocked gas emission (Mills et al. 2015). To investigate whether any maser sources are associated with the arc, we can compare the positions and velocities of the masers with those of the arc. To do this, we first fit the velocity field of the arc parent cluster (see Fig. 1) with a bivariate polynomial (cf. Federrath et al. 2016; Henshaw et al. 2019). The velocity field displayed in Fig. 1 shows a clear gradient, which increases from ∼0 km s$^{-1}$ in the (Galactic) north-east to ∼25 km s$^{-1}$ in the south-west of the cloud, which we fit using

$$v_{mod} = v_0 + \mathcal{G}_l l + \mathcal{G}_b b, \tag{1}$$

where $v_0$ is the systemic velocity of the source, $l$ and $b$ are the Galactic longitude and latitude, and $\mathcal{G}_l$ and $\mathcal{G}_b$ are the longitudinal and latitudinal components of the velocity gradient, respectively. The best-fitting parameters are $v_0 = 14.7$ km s$^{-1}$, and (converting from degrees to physical units) $\mathcal{G}_l = 1.2$ km s$^{-1}$ pc$^{-1}$, and $\mathcal{G}_b = -1.0$ km s$^{-1}$ pc$^{-1}$. We then cross reference the maser catalogue of Mills et al. (2015) against this function, identifying all masers that lie in the range $v_{mod} \pm 6$ km s$^{-1}$. This velocity limit represents ≈2 resolution elements in the ALMA HNCO data. We highlight the 24 masers that are associated with the arc as opaque magenta squares in Fig. 1 (masers outside of this velocity range are shown as semitransparent magenta squares). These masers clearly follow the curvature of the arc, highlighting the association between the arc and
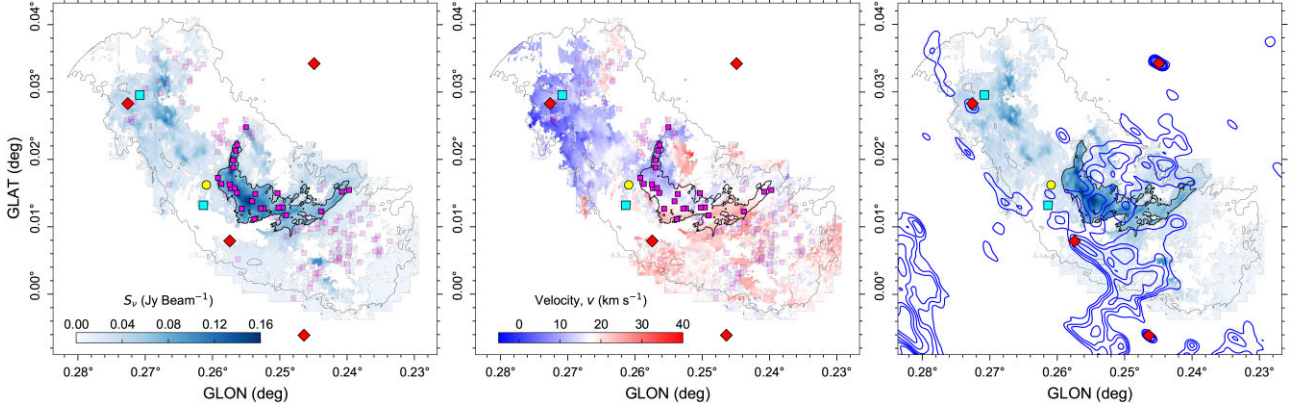
**Figure 1.** Left: The peak flux distribution associated with the arc's parent subcloud identified in Paper I. The colour scale shows the peak amplitude of all Gaussian components associated with the arc's parent subcloud (derived from the fitting of the HNCO data). The thick black contour highlights the arc itself. The thin black contour shows the boundary of G0.253+0.016 estimated from the integrated emission of HNCO. We overlay the location of the $H_2O$ maser identified by Lis et al. (1994) as a yellow circle and the additional $H_2O$ masers identified by Lu et al. (2019a) as cyan squares. H II region candidates from Rodríguez & Zapata (2013) are shown as red diamonds. Purple squares indicate the locations of class I $CH_3OH$ masers and maser candidates identified by Mills et al. (2015). Transparent squares are those which lie outside of a $\pm 6$ km s$^{-1}$ velocity range around a 2D velocity plane fitted to the ACORNS data (see text). Centre: The corresponding centroid velocity map of the arc's parent subcloud. The symbols are equivalent to those in the left-hand panel. Right: The peak flux distribution with the VLA radio continuum data overlaid as blue contours. Contours start at $3\sigma$ ($\sigma = 0.15$ mJy beam$^{-1}$), then $5\sigma$, $7\sigma$, $10\sigma$, $15\sigma$, and $20\sigma$ (Butterfield et al., in preparation).

the shocks traced by the class I $CH_3OH$ masers. In addition to these masers, Mills et al. (2015) noted the presence of more extended, non-masing $CH_3OH$ emission towards the arc. This is suggested to be quasi-thermal or 'quenched' emission (Menten 1991; Mehringer & Menten 1997), indicative of higher gas densities in this region.

In the right-hand panel of Fig. 1, we present the 5 GHz radio continuum emission observed with the VLA (blue contours). A striking feature of this emission is that it appears to fill the cavity traced by the arc. The emission within the arc cavity also connects in projection to a ridge of radio continuum emission that traces the outer (Galactic) eastern edge of the cloud. This latter ridge has been noted in earlier studies and has been attributed to the ionizing influence of a known O4-6 supergiant located towards the (Galactic) south-east of the cloud (Mauerhan et al. 2010; Mills et al. 2015).

Fig. 2 is a histogram of the centroid velocity information extracted in Henshaw et al. (2019). The left-hand panel shows the distribution of centroid velocities for three distinct components. The dark blue histogram shows the arc itself, defined as the region enclosed by the thick black contour in Fig. 1. For comparison, the medium blue histogram shows the arc's parent subcloud, and the light blue histogram shows all of G0.253+0.016 (Henshaw et al. 2019). A Gaussian fit to the dark blue histogram (red dashed Gaussian in Fig. 2) gives a mean velocity of $\langle v \rangle = 17.6$ km s$^{-1}$ with a standard deviation of 4.5 km s$^{-1}$.

### 3.2 A simple geometrical model

To better understand the morphology and dynamics of the arc, we construct a simple model of a tilted ring projected on the plane of the sky (cf. López-Calderón et al. 2016; Callanan et al. 2021). The model is described by five free-parameters: (i) and (ii) the coordinates of the ring centre on the plane of the sky, $\{l_0, b_0\}$, (iii) the radius of the ring, $R_{arc}$, and (iv) and (v) two angles, $\beta$, $\gamma$, that describe the orientation of the ring relative to the plane of the sky (inclination and position angle, see Callanan et al. 2021). Formally, we describe the shape of the ring by constructing a local Cartesian coordinate system centred on the ring, with $\hat{x}$ along the line of sight, and $\hat{y}$ and

$\hat{z}$ aligned with Galactic longitude and latitude. We begin with a ring lying in the $xy$ plane of this coordinate system (i.e. edge-on from our point of view, and at constant Galactic latitude), whose coordinates can be expressed parametrically as $\mathbf{r} = (R_{arc} \cos\theta, R_{arc} \sin\theta, 0)$ with $\theta \in [0, 2\pi]$. The angles $\beta$ and $\gamma$ then represent rotations about the $y$ and $x$ axes of this coordinate system,[3] so the coordinates of the ring become $\mathsf{R}_y(\beta)\mathsf{R}_x(\gamma)\mathbf{r}$, where $\mathsf{R}_x$ and $\mathsf{R}_y$ are the usual rotation matrices for rotations about the $x$ and $y$ axes:

$$\mathsf{R}_y(\beta) = \begin{bmatrix} \cos\beta & 0 & \sin\beta \\ 0 & 1 & 0 \\ -\sin\beta & 0 & \cos\beta \end{bmatrix} \qquad (2)$$

$$\mathsf{R}_x(\gamma) = \begin{bmatrix} 1 & 0 & 0 \\ 0 & \cos\gamma & -\sin\gamma \\ 0 & \sin\gamma & \cos\gamma \end{bmatrix}. \qquad (3)$$

To find the parameters that best describe the arc, we minimize the distance between the image pixels that we identify as being in the arc and the projected arc model. Formally, our procedure is as follows. For any proposed vector of parameters $\mathbf{P}$ describing the arc, we first compute the projected position of the arc in the Cartesian coordinate system defined by the observed image; we denote this projected position $(x_\mathbf{P}(\theta), y_\mathbf{P}(\theta))$, where $\theta$ is a parametric variable that varies from 0 to $2\pi$. The data to which we fit this model consist of the set of $N$ pixels in the image that we have identified as being part of the arc; let $(x, y)_i$ for $i = 1 \dots N$ denote the positions of the centres of these pixels in the image coordinate system. For each pixel $i$, we define the distance to any point on the model arc by

$$d_{i,\mathbf{P}}(\theta) = \sqrt{[x_\mathbf{P}(\theta) - x_i]^2 + [y_\mathbf{P}(\theta) - y_i]^2}, \qquad (4)$$

and we further define $d_{\min,i,\mathbf{P}}$ as the minimum of $d_{i,\mathbf{P}}(\theta)$ on the domain $\theta = [0, 2\pi]$, i.e. $d_{\min,i,\mathbf{P}}$ is the minimum distance from the centre of pixel $i$ to any point on the arc. We define our goodness-of-fit statistic for a proposed set of model parameters $\mathbf{P}$ by $\chi^2(\mathbf{P}) = \sum_{i=1}^{N} d_{\min,i,\mathbf{P}}$,

---

[3]We need not consider rotations about the $z$-axis for reasons of symmetry.
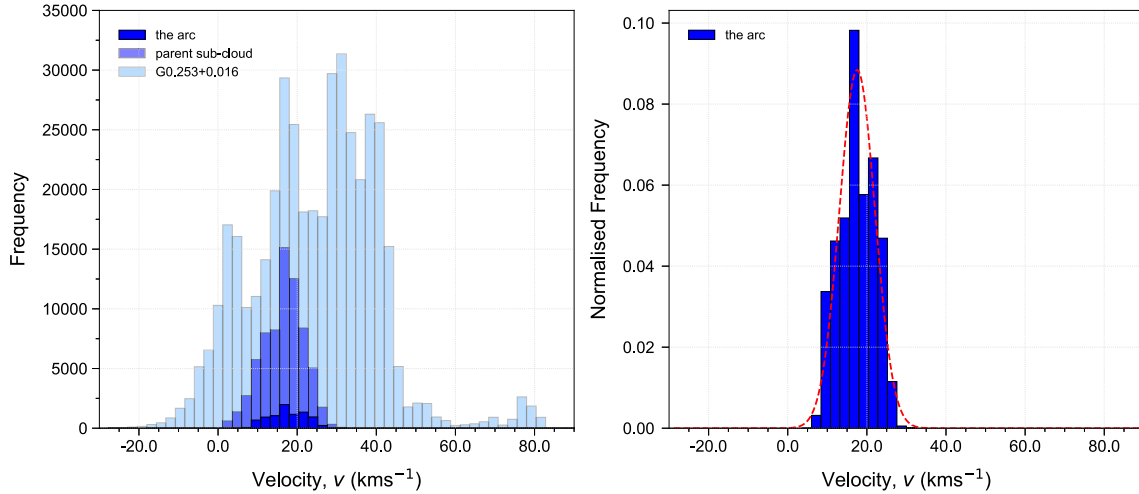
**Figure 2.** Left: Histogram of the centroid velocity measurements associated with G0.253+0.016. The light blue histogram displays all velocities extracted from the HNCO data across G0.253+0.016, medium blue refers to the velocities of the arc's parent subcloud, and dark blue is a histogram of the arc velocities. Right: Normalized histogram of the centroid velocities associated with the arc. We overlay a Gaussian fit to the histogram (red dashed line). The mean velocity is $\langle v \rangle = 17.6 \pm 4.5$ km s$^{-1}$, where the uncertainty here refers to the standard deviation of the distribution.

i.e. the goodness of fit of the model is simply the sum of the squared minimum distances between the arc pixels in the image and the projected arc produced by a given set of model parameters. We find the set of parameters **P** that minimize this objective function using a standard Levenberg–Marquardt minimization method (Newville et al. 2014).

Our best-fitting model geometry is displayed in Fig. 3, where it is overlaid on maps of the peak amplitude and gradient-subtracted velocity field (see Section 3.1) of the arc. The circular model forms an ellipse when projected on the plane of the sky. It is centred on $\{l_0, b_0\} = \{0°248, 0°018\}$ and has a radius $R_{\mathrm{arc}} = 32$ arcsec or $R_{\mathrm{arc}} = 1.3$ pc.[4]

The gradient-subtracted velocity field (see Section 3.1) presented in the right-hand panel of Fig. 3 is quite complex. Broadly speaking, the velocities transition from blueshifted to redshifted and back to blueshifted emission again in the azimuthal direction. Gradients in the radial direction further complicate this picture. However, the azimuthal trend may be produced by the expansion of the arc. We can verify this with our toy model. First, we assume that the arc is expanding radially and second, that the expansion velocity is constant in azimuth in the plane of the arc. Having fixed the geometry, we perform another least-squares fit to determine the expansion velocity, $v_{\mathrm{exp}}$, that best describes the velocity field of the arc. We do this in two ways. In the first method, we include only the expansion velocity as a free parameter in the model. In the second method, we introduce a constant in addition to the expansion velocity that represents the systemic line-of-sight velocity of the arc, $v_{\mathrm{arc},0}$. For the former, we derive $v_{\mathrm{exp}} = 3.3$ km s$^{-1}$. For the latter, we derive $v_{\mathrm{exp}} = 7.9$ km s$^{-1}$ and $v_{\mathrm{arc},0} = -3.1$ km s$^{-1}$. The introduction of the additional free parameter in the second method leads to the factor of ∼2 change in the modelled expansion velocity. This latter model is displayed as the coloured dots in the right-hand panel of Fig. 3 (the colour scale of the dots matches that of the background velocity field). Finally, we introduce a 'control' estimate of the expansion

velocity by simply fitting a Gaussian to the distribution of gradient-subtracted centroid velocities shown in Fig. 1. We then estimate the expansion velocity as the half-width at half-maximum (HWHM) of this distribution, finding $v_{\mathrm{exp}} = 4.2$ km s$^{-1}$. Each of these estimates is highlighted in Fig. 4, which is a position–velocity diagram extracted along the (partial) ellipse shown in Fig. 3 (the 0.0 location is taken to be the lowest Galactic longitude point on the arc). The dot–dashed line reflects our kinematic model with $v_{\mathrm{exp}} = 3.3$ km s$^{-1}$, the dotted line represents the model with $v_{exp} = 7.9$ km s$^{-1}$, and the horizontal lines represent the HWHM approach with $v_{\mathrm{exp}} = 4.2$ km s$^{-1}$.

The uncertainties in this modelling approach are considerable, and the velocity field of the arc is more complicated than that produced by this simplified model. None the less, this simple approach demonstrates the plausibility that the morphology of the arc, as well as its dynamics, may be interpreted as an expanding shell. For the sections that follow, we propagate the uncertainties associated with this modelling into our calculations. We use the mean of the expansion velocities as our fiducial estimate but retain the upper and lower limits for further calculations, $v_{\mathrm{exp}} = 5.2^{+2.7}_{-1.9}$ km s$^{-1}$. Under these assumptions, we can estimate the dynamical age of the arc,

$$t_{\mathrm{dyn}} = \frac{R_{\mathrm{arc}}}{v_{\mathrm{exp}}}. \tag{5}$$

With our best-fitting values $R_{\mathrm{arc}} = 1.3$ pc and $v_{\mathrm{exp}} = 5.2^{+2.7}_{-1.9}$ km s$^{-1}$, the estimated dynamical age is $t_{\mathrm{dyn}} \approx 2.4^{+0.8}_{-1.4} \times 10^5$ yr (assuming a constant expansion velocity).

### 3.3 Mass, energy, and momentum

With an estimate of the expansion velocity, we can estimate the energy and momentum associated with the arc. To do this, we first estimate a mass using dust continuum emission. We derive the total mass of the arc within the black contour presented in Fig. 3 from the 3 mm dust continuum emission from ALMA Cycle 0, first presented by Rathborne et al. (2014b):

$$M_{\mathrm{arc}} = \frac{d^2 S_\nu R_{\mathrm{g2d}}}{\kappa_\nu B_\nu(T_{\mathrm{d}})}, \tag{6}$$

[4]If we would have simply fitted the arc as a circle on the plane of the sky, we would have obtained $\{l, b\} = \{0°250, 0°018\}$ and a radius of $R_{\mathrm{arc}} = 25.8$ arcsec or $R_{\mathrm{arc}} = 1.0$ pc.
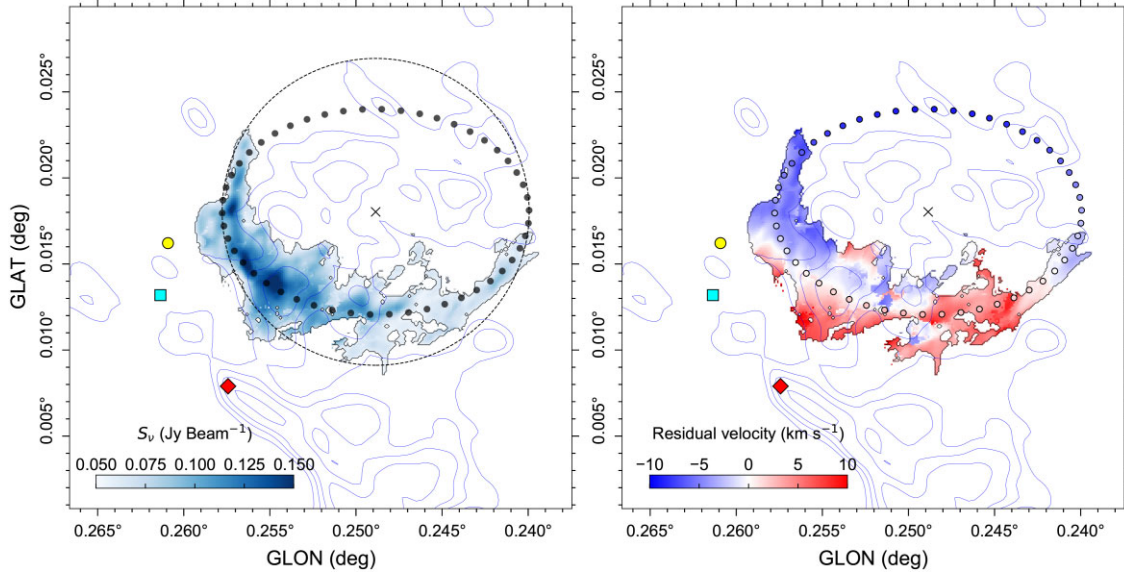
**Figure 3.** Left: The colour scale indicates the peak amplitude of the Gaussian components associated with the arc (derived from the fitting of the HNCO data). The thick black dotted circle indicates our best-fitting toy model of an expanding ring. It is centred on $\{l_0, b_0\} = \{0.248°, 0.018°\}$ and has a radius $R_{arc} = 32$ arcsec or $R_{arc} = 1.3$ pc. The dashed circle has an equivalent radius and is shown for reference. Right: The velocity field of the arc after subtracting the bulk motion of the arc's parent subcloud. The dotted circle once again shows the geometry of our best-fitting toy model, however, here the colour of the dots indicates the expansion of the ring (see text for details). The contours are equivalent to those in Fig. 1.
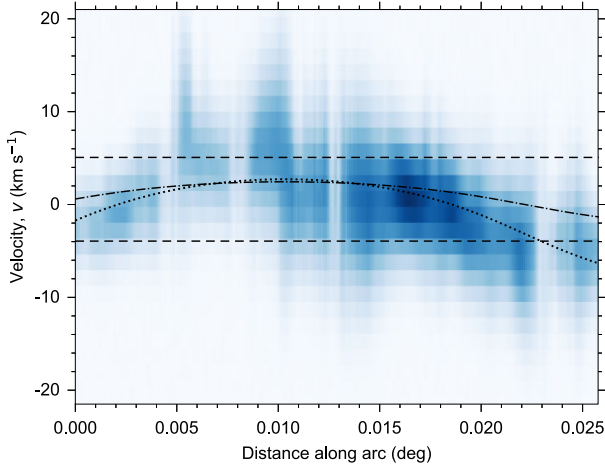


**Figure 4.** A position–velocity diagram extracted along the dotted ellipse presented in Fig. 3. The 0.0 location is taken to be the lowest Galactic longitude point on the arc. The colour scale reflects the peak amplitude of the HNCO emission. The lines represent different models for the kinematics of the arc velocity field presented in the right-hand panel of Fig. 3. The horizontal dashed lines represent the most simplistic approach to estimating the expansion velocity, and reflect the HWHM of the gradient-subtracted velocity distribution (see text for details), $v_{exp} = 4.2$ km s$^{-1}$. The dot–dashed and dotted lines correspond to the model velocity fields described in Section 3.2. The former of these models has a constant expansion velocity of $v_{exp} = 3.3$ km s$^{-1}$. The latter also has constant expansion velocity, this time $v_{exp} = 7.9$ km s$^{-1}$, but the model also includes a constant line-of-sight velocity of $v_{0, arc} = -3.1$ km s$^{-1}$.

where $d$ is the distance to the source, $S_\nu$ is the integrated flux density (in Jy), $R_{g2d}$ is the gas-to-dust ratio, $\kappa_\nu$ is the dust opacity per unit mass at a frequency $\nu$, and $B_\nu(T_d)$ is the Planck function at a dust temperature, $T_d$. We adopt a dust opacity per unit mass

$\kappa_\nu = \kappa_0(\nu/\nu_0)^\beta$ with $\kappa_0 = 0.899$ cm$^2$g$^{-1}$, valid for the moderately coagulated thin ice mantle dust model of Ossenkopf & Henning (1994) with densities of $10^6$ cm$^{-3}$ at $\nu_0 = 230$ GHz. We adopt $\beta = 1.75$ following Battersby et al. (2011), giving an opacity $\kappa_\nu \approx 0.21$ cm$^2$g$^{-1}$ at a frequency of $\sim$93 GHz.

Two considerable sources of uncertainty in our mass estimate are the dust temperature and the gas-to-dust ratio, $R_{g2d}$. For the former, G0.253+0.016 overall shows low dust temperatures of the order $\sim$20 K (Longmore et al. 2012; Tang, Wang & Wilson 2021). Marsh et al. (2016) find that the dust associated with the arc consists of a cool ($<$20 K) and a warm component (up to $\sim$50 K). In terms of the gas temperature, Mills et al. (2018, see also Ginsburg et al. 2016; Krieger et al. 2017) also find evidence from HC$_3$N emission in G0.253+0.016 for two distinct components, one low-excitation, low-density ($n \sim 10^3$ cm$^{-3}$; $T \sim 25$–50 K) and one high-excitation, high-density ($n \sim 10^5$ cm$^{-3}$; $T \sim 60$–100 K). The gas temperature in Galactic Centre clouds is typically higher than the dust temperature (Krieger et al. 2017) and modelling indicates that even at densities of $10^5$ cm$^{-3}$, the gas and dust are unlikely to be in thermal equilibrium (Clark et al. 2013). The uncertainty on the dust temperature is most likely a factor of 2. Moreover, given that the metallicity in the Galactic Centre is approximately twice solar (Mezger et al. 1979; Feldmeier-Krause et al. 2017; Schultheis et al. 2019, 2021), the gas-to-dust ratio is likely lower by a similar factor (Longmore et al. 2013a; Giannetti et al. 2017).

Combining the above uncertainties, we estimate that the arc has a mass of $M_{arc} \sim 2700^{+3000}_{-1400}$ M$_\odot$, where the fiducial value corresponds to $T = 50$ K and $R_{g2d} = 100$ (or $T = 25$ K and $R_{g2d} = 50$). We caution that this still likely represents a strict upper limit to the mass of the arc because there are multiple velocity components along the line of sight in this location, which are not accounted for in mass derivations from continuum observations. Importantly, the arc spatially overlaps with the dominant subcloud in G0.253+0.016, which likely contains most of the mass (Henshaw et al. 2019). Therefore, although the
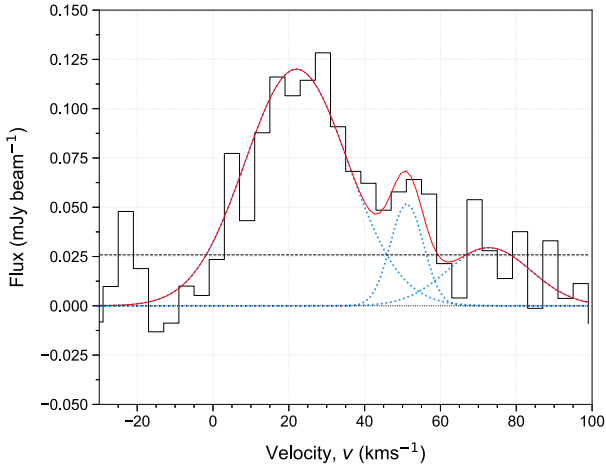
**Figure 5.** RRL spectrum extracted from within the circle presented in Fig. 3. This spectrum was created by stacking a total of seven RRLs, namely H114$\alpha$, H113$\alpha$, H110$\alpha$, H109$\alpha$, H101$\alpha$, H100$\alpha$, and H99$\alpha$. The horizontal dotted line indicates the 0.0 line and the horizontal dashed line indicates $3.0 \times \sigma_{\rm rms}$ (0.026 mJy beam$^{-1}$). The red curve indicates a three-component Gaussian fit to the data. The component at lower velocities has a centroid velocity of $22.0 \pm 1.4$, closely matching the velocity of the molecular component of arc (Fig. 2).

uncertainty on the mass derived from continuum observations is of the order a factor of $\sim$2, this additional consideration means that the uncertainty could be higher.

With estimates for the mass and expansion velocity in hand, we can now estimate the kinetic energy and momentum of the arc using

$$E_{\rm arc} = \frac{1}{2} M_{\rm arc} v_{\rm exp}^2 \qquad (7)$$

and

$$p_{\rm arc} = M_{\rm arc} v_{\rm exp}, \qquad (8)$$

finding $E_{\rm arc} \sim 0.7^{+2.8}_{-0.6} \times 10^{48}$ erg and $p_{\rm arc} \sim 1.4^{+3.1}_{-1.0} \times 10^4\,\mathrm{M_\odot}$ km s$^{-1}$, respectively. We discuss these values in more detail in Section 4.

### 3.4 On the nature of the radio emission and the association between the arc and the ionized gas

Radio continuum emission is detected throughout the arc cavity in projection (Fig. 1). However, as discussed in Section 3.1, the emission extends further to the (Galactic) south and east. While it is certainly possible that the radio continuum emission is physically related to the arc, projection effects may be important. To investigate whether the ionized gas is physically associated with the molecular arc, we extract an RRL spectrum from the region marked with a dotted circle in Fig. 3. In practice, we stack the emission from a total of seven RRL transitions, namely H114$\alpha$, H113$\alpha$, H110$\alpha$, H109$\alpha$, H101$\alpha$, H100$\alpha$, and H99$\alpha$. The resulting spectrum is displayed in Fig. 5. In addition to stacking, we have smoothed the native spectral resolution of the stacked spectrum by a factor of 4 to further increase the signal-to-noise ratio. We fit the smoothed spectrum using a multicomponent Gaussian model using the standalone fitter functionality of SCOUSEPY (Henshaw et al. 2019). This procedure uses derivative spectroscopy to determine the number of emission features within each spectrum and their properties (i.e. their peak amplitude, velocity centroid, and width; Lindner et al. 2015; Riener et al. 2019). Using a Gaussian smoothing kernel of standard deviation 1.5 channels, and ensuring

that all identified components are above a signal-to-noise ratio of 3, this method predicts a three-component model. The brightest component has a centroid velocity of $22.0 \pm 1.4$ km s$^{-1}$ and has a velocity dispersion of $13.6 \pm 1.5$ km s$^{-1}$. This velocity is redshifted with respect to the mean of the arc centroid velocity distribution (17.6 km s$^{-1}$), but is consistent to within one standard deviation and is importantly inconsistent with the other subclouds associated with G0.253+0.016 (Henshaw et al. 2019). Note that the combination of the broad lines, spectral smoothing, and the narrow bandwidth make it difficult to determine if the two lower brightness emission features are significant. However, they are located at higher velocity and are therefore not relevant here. The consistency in velocity between the RRL emission and the molecular gas tracing the arc, in addition to the spatial relationship between the radio continuum emission and the arc cavity, leads us to conclude that the molecular gas and ionized gas are most likely related.

To help better understand the nature of the ionized gas, we estimate the electron density, recombination time, and Lyman continuum ionizing flux. The morphological and kinematic match between the radio emission presented here (continuum and RRL emission, respectively) and the arc (Fig. 3) gives us confidence that the two are physically related. However, we note that G0.253+0.016 lies close in projection to both of thermal and non-thermal radio sources, in particular the arched radio filaments that are oriented perpendicular to the Galactic plane (Morris & Yusef-Zadeh 1989; Yusef-Zadeh 1989). G0.253+0.016 also overlaps in projection with the prominent supernova remnant G0.30+0.00 (Kassim & Frail 1996; LaRosa et al. 2000), and an additional candidate supernova remnant lies directly to the Galactic west of the arc (Ponti et al. 2015). The contribution of non-thermal emission to the radio continuum flux may therefore be non-negligible. We therefore estimate the electron density, recombination time, and Lyman continuum ionizing flux in two ways (i) assuming that the radio continuum flux is produced entirely by free–free emission, which provides our upper limit and (ii) using the RRL emission to self-consistently predict what the expected free–free continuum flux would be.

The total integrated continuum flux within the arc cavity (see the circle in Fig. 3) is $\sim$80 mJy. This provides our strict upper limit on the free–free emission. The measured RRL integrated intensity in Fig. 5 is 5.2 mJy km s$^{-1}$ (4.6 K km s$^{-1}$). Assuming that the RRLs are optically thin and in local thermodynamic equilibrium (typical departure coefficients $\beta_n$ are very close to unity for H99-114$\alpha$; Storey & Hummer 1995), we can use equation (14.29) of Wilson, Rohlfs & Hüttemeister (2009, 5th ed.) to derive the line-to-continuum ratio of the RRLs, $T_{\rm L}/T_{\rm C}$

$$\frac{T_{\rm L}}{T_{\rm C}} \frac{\delta v}{\mathrm{km\,s^{-1}}} = \frac{6.985 \times 10^3}{a(v, T_{\rm e})} \left[\frac{v}{\mathrm{GHz}}\right]^{1.1} \left[\frac{T_{\rm e}}{\mathrm{K}}\right]^{-1.15} (1 + y_{\rm He})^{-1} \qquad (9)$$

where $a(v, T_{\rm e})$ is the Gaunt factor, assumed to be unity, and $y_{\rm He} = N(\mathrm{He}+)/N(\mathrm{H}+)$, the ratio of helium to hydrogen ions, is assumed to be 0.1. We determine $T_{\rm L}/T_{\rm C} \approx 2.5$ km s$^{-1}$ for $T_{\rm e} = 5000$ K. From this ratio we determine that the expected continuum flux is $\approx$1 mJy (cf. $\sim$80 mJy derived from the continuum). This calculation indicates that the continuum likely suffers contamination from non-thermal emission, and the estimated continuum flux from the RRL emission provides a lower bound to the contribution from free–free emission.

The electron density within the shell (assuming that the ionized gas fills the volume of the shell bounded by the arc) is (Mezger & Henderson 1967; Rubin 1968)

$$n_{\rm e} = 2.3 \times 10^6 \left[\frac{S_v}{\mathrm{Jy}}\right]^{0.5} \left[\frac{v}{\mathrm{GHz}}\right]^{0.05} \left[\frac{T_{\rm e}}{\mathrm{K}}\right]^{0.175} \left[\frac{d}{\mathrm{pc}}\right]^{-0.5} \left[\frac{\theta}{\mathrm{arcsec}}\right]^{-1.5} \mathrm{cm^{-3}}, \quad (10)$$

where $S_\nu$ is the integrated flux density at a frequency $\nu$ (5 GHz), $T_e$ is the electron temperature (which we assume to be $T_e = 5 \times 10^3$ K, relevant for the electron temperature in Galactic Centre H II regions; Lang, Goss & Wood 1997; Deharveng et al. 2000; Law et al. 2009), $d$ is the source distance, and $\theta = 2R = 64$ arcsec refers to the angular size of the source. The recombination time is $t_{rec} = 1/(n_e \alpha_B)$, where $\alpha_B$ is the hydrogen recombination coefficient, which we assume is $\alpha_B = 4.5 \times 10^{-13}$ cm$^3$ s$^{-1}$ (valid for an assumed temperature of $5 \times 10^3$ K; Draine 2011a). For the lower and lower bounds on the free–free emission, we derive a range in electron density of $n_e \approx$ 10–93 cm$^{-3}$. The corresponding range in recombination time is $t_{rec} \approx$ 760–7000 yr.

The Lyman continuum photon injection rate needed to balance recombinations is (Mezger & Henderson 1967; Rubin 1968):

$$N_{LyC} = 8.40 \times 10^{40} \left[\frac{S_\nu}{Jy}\right]\left[\frac{\nu}{GHz}\right]^{0.1}\left[\frac{T_e}{10^4 K}\right]^{-0.45}\left[\frac{d}{pc}\right]^2 s^{-1}. \quad (11)$$

Inserting numerical values, we derive a range for the Lyman continuum ionizing flux of $N_{LyC} \approx 10^{46.0}$–$10^{47.9}$ photons s$^{-1}$. The Lyman continuum photon rate gives us some insight into the type of source that may be driving this emission. Assuming that the emission is produced by a single zero-age main-sequence star, the bounds of our derived $N_{LyC}$ values correspond to stars of spectral type B1-O8.5, with corresponding masses of 12–20 M$_\odot$ (Panagia 1973; Smith, Norris & Crowther 2002; Martins, Schaerer & Hillier 2005; Armentrout et al. 2017). We conclude that the driving source of the continuum may be a high-mass star. In the following sections, we discuss whether such a star is the likely driving source of the arc.

## 4 DISCUSSION

In the case of massive stellar clusters ($M > 10^3$ M$_\odot$), the energetic processes are dominated by three main forms of feedback: ionizing radiation, stellar winds, and supernovae (Krumholz et al. 2014). Stellar feedback plays an integral role in shaping the interstellar medium (ISM) and regulating star formation at the centre of the Galaxy (Kruijssen et al. 2014; Krumholz, Kruijssen & Crocker 2017; Armillotta et al. 2019; Barnes et al. 2020; Sormani et al. 2020; Tress et al. 2020). Although the star formation rate is low in the CMZ (Longmore et al. 2013a), the Galactic Centre star-forming regions (e.g. Sgr B2 and Sgr A) are among the most luminous in the Milky Way. The results presented in the previous section, specifically the morphology and dynamics of the molecular arc and its apparent physical association with the ionized gas emission, suggest that the arc may be the result of stellar feedback. This conclusion is at odds with previous works suggesting that the arc may have been generated during a cloud–cloud collision (Higuchi et al. 2014). This conclusion is also in tension with the generally accepted view that G0.253+0.016 is largely quiescent, with only a single known site of confirmed active star formation (Walker et al. 2021). In the following sections, we discuss the possible origins of the arc, assuming that it is generated by stellar feedback, before addressing the question of whether or not we would expect to detect its progenitor star towards G0.253+0.016.

### 4.1 Is the arc a shell swept up by the wind of an interloper star?

One hypothesis that would be consistent with the quiescent picture of G0.253+0.016, is that the arc represents a shell swept up by the wind of an interloper star. High-mass stars possess powerful winds and the CMZ is unique in our Galaxy in that there is a rich population of 'field' high-mass stars distributed throughout (Mauerhan et al. 2010; Dong et al. 2011; Clark et al. 2021). The origin of this population is

unclear. In general, the lifetimes of molecular clouds in the CMZ are short ($\sim$1 Myr; Henshaw, Longmore & Kruijssen 2016b; Jefferson et al. 2018). Clouds are destroyed by powerful stellar feedback (Barnes et al. 2020) and their emergent stellar populations contribute to the field. Another possibility is that some of this population results from the tidal stripping of, or from stellar interactions within the CMZ's massive clusters the Arches and Quintuplet (Habibi, Stolte & Harfst 2014). Irrespective of their origins, the impact that these high-mass field stars have on the surrounding ISM is not well understood (although see Simpson et al. 2018, 2021).

We can crudely estimate the likelihood that the star represents an interloper using simplistic assumptions based on the known properties of the CMZ. If we take the approximate present-day star formation of the CMZ, $\sim$0.1 M$_\odot$ yr$^{-1}$ (which has been more or less constant over the past several Myr; Longmore et al. 2013a; Barnes et al. 2017), and make the assumption that the vast majority of this star formation is confined to a torus with major and minor radii of $\sim$100 and $\sim$10 pc, respectively (Molinari et al. 2011; Kruijssen, Dale & Longmore 2015; Henshaw et al. 2016a), the expected volumetric star formation rate is of the order $\sim$0.5 M$_\odot$ Myr$^{-1}$ pc$^{-3}$. First consider a scenario where the interloper is an O star with a lifetime $\approx$4 Myr. Assuming that a single 16–20 M$_\odot$ star is produced for every $\sim$500 M$_\odot$ cluster produced (assuming a standard Kroupa 2001 initial mass function; IMF), the density of 16–20 M$_\odot$ stars is $\rho_* = 1/250$ pc$^{-3}$, and the expected number within the volume of G0.253+0.016, assuming a cross-sectional area $A \sim 17$ pc$^2$ and a depth $L = 4.7$ pc (Federrath et al. 2016), is $\langle N \rangle = AL\rho_* \approx 0.3$. This is high enough that we must consider the possibility that an interloper might be responsible for the arc. In the alternative scenario where the interloper is a B star, the expected number is even larger, since B stars are both more common and live longer.

Numerical simulations show that the winds from runaway O and B stars can sweep up a dense shell as they pass through molecular clouds (Mackey et al. 2015). It is tempting to speculate that such a star may have been exiled from the Arches or Quintuplet (Portegies Zwart et al. 2010). This possibility has been discussed in relation to both Sgr B1 (Simpson et al. 2018) and the Sgr A-H group of H II regions (Hankins et al. 2019). The Arches cluster in particular is located to the (Galactic) west of G0.253+0.016 and has a projected distance of just $\sim$20 pc. The Arches is a young ($2-4$ Myr; Najarro et al. 2004; Martins et al. 2008) massive ($4-6 \times 10^4$ M$_\odot$; Clarkson et al. 2012) cluster containing a large number of high-mass stars (Hosek et al. 2015).

To explore this hypothesis further, we can examine the size of the arc in more detail. As the relative velocity between the runaway star and the ambient medium increases, the characteristic size of the swept-up shell driven by the star's wind decreases (Mackey et al. 2015). The scale of the bow shock produced, the stand-off distance, is defined as the point where the momentum flux of the stellar wind balances the momentum flux of the ambient medium, and is given by (Baranov, Krasnobaev & Kulikovskii 1971; Green et al. 2019)

$$R_{st} = \sqrt{\frac{\dot{M}v_\infty}{4\pi\rho_0\left(v_*^2 + c_s^2\right)}} \quad (12)$$

where $\dot{M}$ is the stellar wind mass-loss rate, $v_\infty$ is the terminal wind velocity, $\rho_0$ is the density of the ambient medium, $v_*$ is the velocity of the star with respect to the ambient medium, and $c_s$ corresponds to the sound speed, in this case in the molecular phase. This is because the bow shock is expected to trap the ionization front for the strong wind and dense ISM derived above (Mac Low et al. 1991; Arthur &

Hoare 2006), in which case the bow shock expands into molecular gas.

Using equation (12), we can ask the question: What size shell could be produced by the type of high-mass star needed to stimulate the ionized emission observed within the arc cavity? To address this question, we first estimate the mass-loss rate and terminal wind velocity of the high-mass star. The limiting case, i.e. the star that is capable of producing a shell with the largest radius, is given by the upper end of our mass limit derived in Section 3.4. For O stars which span the range of spectral types consistent with our estimated Lyman continuum photon rate of $N_{\rm LyC} = 10^{47.9}$ photons s$^{-1}$ (O9.5, O9, O8.5), Martins et al. (2005, see their table 1) provide stellar masses ($M/M_\odot = \{16.46, 18.03, 19.82\}$), luminosities ($\log L/L_\odot = \{4.62, 4.72, 4.82\}$), and effective temperatures ($T = \{30\,488, 31\,524, 32\,522\}$ K). We can use this information to determine the mass-loss rate using the metallicity-dependent relationship described in Vink, de Koter & Lamers (2001). We derive mass-loss rates for two metallicities (consistent with our mass calculations in Section 3.3), namely solar and twice solar, finding $\dot{M}(Z/Z_\odot = 1) = \{0.3, 0.4, 0.7\} \times 10^{-7}\,M_\odot$ yr$^{-1}$ and $\dot{M}(Z/Z_\odot = 2) = \{0.5, 0.8, 1.2\} \times 10^{-7}\,M_\odot$ yr$^{-1}$, respectively. We determine the terminal wind velocity assuming $v_\infty = 2.6 v_{\rm esc}$ (McLeod et al. 2019, see also Barnes et al. 2020), where $v_{\rm esc}$ is the escape velocity obtained from Muijres et al. (2012, $v_{\rm esc} = \{892, 908, 923\}$ km s$^{-1}$). Although our upper limit on the stellar mass represents the limiting case for this scenario, it is worth noting that both observations (Mokiem et al. 2007) and simulations (Offner & Arce 2015) show that the mass-loss rates from early-type B stars predicted from models of wind launching (Vink et al. 2001) can be underestimated by orders of magnitude (see fig. 3 of Smith 2014). In some cases, the mass-loss rates can be as high as the model-predicted mass-loss rates of the more massive O-stars considered here (albeit with moderately slower winds).

Next, we use the mass of the arc to estimate the initial density of the cloud prior to the star's passage, assuming this gas originally filled the volume defined by the radius of the arc. For $M_{\rm arc} \sim 2700^{+3000}_{-1400}\,M_\odot$, we find $\rho_0 = 3M_{\rm arc}/4\pi R_{\rm arc}^3 = 2.1^{+2.3}_{-1.1} \times 10^{-20}$ g cm$^{-3}$, corresponding to a number density $\sim 0.9^{+1.0}_{-0.5} \times 10^4$ cm$^{-3}$ (which is comparable to the mean density of G0.253+0.016; Federrath et al. 2016; Mills et al. 2018). Finally, we assume $v_* = v_{\rm exp} = 5.2^{+2.7}_{-1.9}$ km s$^{-1}$ and $T = 50$ K (Section 3.3), such that $c_{s,\rm mol} = 0.42$ km s$^{-1}$, and compute stand-off distances spanning the extremes of this parameter space. The smallest (largest) stand-off distance is set by the upper (lower) limits in the stellar wind properties and the lower (upper) limits in density and $v_*$. The range in parameters described above produces stand-off distances of the order 0.01–0.1 pc. The predicted size of the shell is therefore at least an order of magnitude smaller than the observed size of the arc.

Looking at this another way, for the star to plausibly be an interloper, it must be able to move a distance of order $L = 4.7$ pc within the star's lifetime, $t_*$, otherwise it is likely that the star was born right next to the cloud. The maximum stand-off distance (for a fixed mass-loss rate and wind speed) is given by the lowest possible relative velocity between the star and the cloud. Assuming a lifetime of $t_* \sim 20$ Myr (the limiting case is given by the longest lifetime, and therefore the B1 star; Hurley, Pols & Tout 2000), this sets a minimum velocity of $v_{\rm min} = L/t_* \sim 0.2$ km s$^{-1}$, which in turn gives a maximum standoff distance of $R_{\rm st} = 0.8$ pc (assuming the upper limits in the stellar wind properties and the lower limit in density), which is smaller than what we observe.

In summary, it is difficult to reconcile the fiducial mass and radius estimates of the arc with those predicted assuming that the arc is a swept up shell driven by a stellar wind of a $\approx$12–20 $M_\odot$ interloper star

moving relative to the cloud. Reconciliation may be possible if: (i) our assumed mass-loss rate and wind velocity are underestimated and (ii) both $\rho_0$ and $v_*$ are overestimated. Regarding the former scenario, some of the 'field' high-mass stars located within the Galactic Centre are more evolved Wolf–Rayet (WR) stars (Mauerhan et al. 2010; Dong et al. 2011; Clark et al. 2021). WR stars have powerful stellar winds, with mass-loss rates that can be 100× that of O stars. However, they are also more luminous, with Lyman continuum ionizing fluxes that are at least an order of magnitude greater than our upper limit derived in Section 3.4 ($N_{\rm NLyC} > 48.6$; Crowther 2007). Therefore, it is unlikely that an interloper WR is generating the arc. Regarding the latter scenario, assuming $v_* = v_{\rm exp}$, the ambient density would have to be $\sim$3 orders of magnitude lower than our fiducial value estimated above (since $R_{\rm st} \propto \rho_0^{-1/2}$). This would imply a swept-up mass so small that the arc would be undetectable in dust emission in the current observations. Therefore, a reduction in both $\rho_0$ and $v_*$ would be needed to reproduce the observed morphology of the arc. Better mass constraints on the arc would help to conclusively rule out this scenario. As discussed in Section 3.3, it is not implausible that the mass estimate that we derive for the arc from dust continuum emission is overestimated, particularly if the bulk of that mass is attributed to a spatially overlapping but unrelated part of the cloud (Henshaw et al. 2019).

### 4.2 Is the arc the result of stellar feedback from in situ star formation?

An alternative hypothesis to that presented in Section 4.1 is that the arc may be the result of stellar feedback associated with *in situ* star formation within G0.253+0.016. To test this hypothesis, we compare the morphology and dynamics of the arc to analytical prescriptions describing the expansion of H II regions.

#### 4.2.1 Thermal expansion of an H II region

The analytical expression for radial expansion of an H II region driven purely by thermal pressure (i.e. with negligible contributions from radiation pressure[5] and stellar winds) is given (Spitzer 1978)

$$R_{\rm Sp}(t) = R_{\rm s}\left(1 + \frac{7}{4}\frac{c_{\rm s,i}t}{R_{\rm s}}\right)^{4/7},\tag{13}$$

where $c_{\rm s,i}$ is the sound speed in the ionized gas, $t$ is the age of the H II region, and $R_{\rm s}$ is the Strömgren radius. The sound speed in the ionized gas is

$$c_{\rm s,i} = \sqrt{2.2\frac{k_{\rm B}T_{\rm i}}{\mu m_{\rm H}}},\tag{14}$$

where $k_{\rm B}$ is the Boltzmann constant, $T_{\rm i}$ is the temperature of the ionized gas, $\mu$ is the mass per hydrogen nucleus in units of $m_{\rm H}$.

---

[5]Note that throughout this discussion we neglect radiation pressure from our analysis. Radiation pressure is only important compared to ionized gas pressure when the radius of the H II region is below a characteristic radius defined by $R_{\rm ch} = 0.06 f_{\rm trap}^2 S_{49}$ pc (Krumholz & Matzner 2009), where $f_{\rm trap}$ represents the factor by which the radiation-pressure force is enhanced by trapping of energy within the expanding shell, and $S_{49}$ is the ionizing luminosity in units of $10^{49}$ s$^{-1}$. Taking the upper limit of our range for the ionizing luminosity $N_{\rm LyC} = 10^{47.9}$ photons s$^{-1}$ (Section 3.4), gives, $R_{\rm ch} \approx 5 \times 10^{-3} f_{\rm trap}^2$, which is much smaller than the radius of the arc unless $f_{\rm trap} > 16$. We therefore conclude that radiation pressure is not the likely driving source of the arc.

The factor of 2.2 arises because there are 2.2 free particles per H nucleus (0.1 He per H, and 1.1 electrons per H; Krumholz 2017). Assuming an ionized gas temperature of $T_i = 5 \times 10^3$ K (Lang et al. 1997; Deharveng et al. 2000; Law et al. 2009), $c_{s,i} \approx 8$ km s$^{-1}$. The Strömgren radius is

$$R_s = \left( \frac{3 N_{LyC} \mu^2 m_H^2}{4(1.1)\pi \alpha_B \rho_0^2} \right)^{1/3}, \tag{15}$$

where we have used the formalism from Krumholz (2017, their equation 7.24). Here, if $\mu = 1.4$, the mean mass per hydrogen nucleus in the gas in units of $m_H$ and $\rho_0$ is the initial density before the photoionizing stars turn on, then $n_p = \rho_0/\mu m_H$ and $n_e = 1.1 \rho_0/\mu m_H$ with the factor of 1.1 coming from assuming that He is singly ionized and from a ratio of 10 He nuclei per H nucleus. Following Section 4.1, we present here only the limiting case and assume $N_{LyC} = 10^{47.9}$ photons s$^{-1}$. Combining with an initial density $\rho_0 = 2.1^{+2.3}_{-1.1} \times 10^{-20}$ g cm$^{-3}$ (Section 4.1), the estimated Strömgren radius is $R_s \approx 0.05^{+0.03}_{-0.02}$ pc.

We can use equation (13) to estimate the time it would take for an H II region to expand to the observed radius of the arc,

$$t_{Sp} = \frac{4}{7} \frac{R_s}{c_{s,i}} \left[ \left( \frac{R_{Sp}}{R_s} \right)^{7/4} - 1 \right]. \tag{16}$$

The corresponding velocity with which the H II region expands is given

$$v_{Sp}(t) = c_{s,i} \left( 1 + \frac{7 c_{s,i} t}{4 R_s} \right)^{-3/7}. \tag{17}$$

Equating $R_{Sp} = R_{arc}$, we find that the estimated age of the H II region would be $t_{Sp} = 1.0^{+0.4}_{-0.3} \times 10^6$ yr. After $\sim 1$ Myr, the corresponding expansion velocity is expected to be $v_{Sp} = 0.7^{+0.3}_{-0.2}$ km s$^{-1}$.

In Fig. 6, we show the time evolution of both the radial expansion (top panel) and the velocity (bottom panel) predicted by the Spitzer (1978; blue dotted lines) model. The two curves (blue dotted lines) represent the upper and lower limits on the radial evolution. These limits come from the upper and lower limits on the mass and therefore density (see equation 15). The shaded region therefore represents the range of parameter space spanned by our estimates of the physical properties. We also include in this figure the model described in Hosokawa & Inutsuka (2006), which also describes thermal expansion but with a slight modification (red dot–dashed lines):

$$R_{H\&I}(t) = R_s \left( 1 + \frac{7}{4} \sqrt{\frac{4}{3}} \frac{c_{s,i} t}{R_s} \right)^{4/7}. \tag{18}$$

Using the Hosokawa & Inutsuka (2006) model, the predicted age and velocity of the H II region are $t_{H\&I} = 0.9^{+0.3}_{-0.3} \times 10^6$ yr and $v_{H\&I} = 0.8^{+0.3}_{-0.2}$ km s$^{-1}$, respectively.

As an H II region expands, the photoionized gas in its interior exerts a pressure force and delivers outward radial momentum and kinetic energy to the swept-up shell. Krumholz (2017, their equation 7.36) shows that the momentum delivered to the ambient medium, assuming a spherical H II region and an ionized gas temperature of $10^4$ K, is

$$p = 1.5 \times 10^5 \left[ \frac{n_H}{10^2 \, cm^{-3}} \right]^{-1/7} \left[ \frac{N_{ly}}{10^{49} \, s^{-1}} \right]^{4/7} \left[ \frac{t}{10^6 \, yr} \right]^{9/7} \left[ \frac{T_e}{10^4 \, K} \right]^{-8/7} \times$$
$$M_\odot \, km \, s^{-1}, \tag{19}$$

where $n_H$ is the number density of H nuclei in the ambient medium into which the H II region is expanding, and $t$ is its age. The expected kinetic energy of the swept-up shell is (Krumholz 2017,
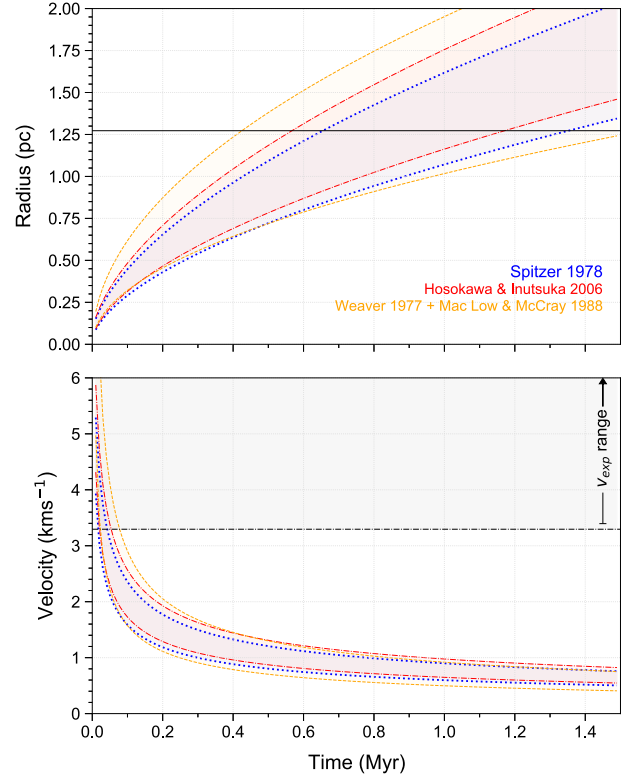


**Figure 6.** The top panel shows analytical predictions for the time evolution of the radii of expanding H II regions from various models (see text for details). The blue dotted curve indicates expansion driven by the thermal pressure of photoionized gas Spitzer (1978). The red dot–dashed curve is the same but with a slight modification from Hosokawa & Inutsuka (2006). The orange dashed curves describe the radial expansion driven by stellar winds for stars of different spectral types consistent with our measurement of $N_{LyC}$ (Weaver et al. 1977; Mac Low & McCray 1988). The horizontal black line represents the radius of the arc $R_{arc} = 1.3$ pc. The bottom panels show the time evolution of the expansion velocity. The black shaded region indicates the range of expansion velocity derived from the different methods presented in Section 3.2 (note that this has been truncated for clarity, as indicated by the black arrow). The horizontal dot–dashed line reflects the lower limit of the expansion velocity estimates shown in Fig. 4.

equation 7.35)

$$E = 8.1 \times 10^{47} \left[ \frac{n_H}{10^2 \, cm^{-3}} \right]^{-10/7} \left[ \frac{N_{ly}}{10^{49} \, s^{-1}} \right]^{5/7} \left[ \frac{t}{10^6 \, yr} \right]^{6/7} \left[ \frac{T_e}{10^4 \, K} \right]^{10/7} \times$$
$$erg. \tag{20}$$

We can use the predicted age of the H II region therefore to evaluate the momentum and energy at $t = t_{Sp}$. Using our fiducial estimates $N_{ly} = 10^{47.9}$ s$^{-1}$ (Section 3.4), $\rho_0 = 2.1^{+2.3}_{-1.1} \times 10^{-20}$ g cm$^{-3}$ ($n_H \sim 0.9^{+1.0}_{-0.5} \times 10^4$ cm$^{-3}$), and $T_e = 5 \times 10^3$ K, we find $p = 3.4^{+2.7}_{-1.5} \times 10^4$ M$_\odot$ km s$^{-1}$ and $0.6^{+1.7}_{-0.5} \times 10^{44}$ erg, respectively.

The above predictions are in considerable tension with the observations. The predicted age of the H II region, implied by the radius of the arc, is almost an order of magnitude greater than the arc's estimated dynamical age (which assumes that the expansion velocity has been constant over this time; Section 3.2). Although the predicted momentum only differs from our measured value by a factor of 2–3, the predicted velocity and energy show considerably more tension with the measured quantities, differing by factors of $\sim 1$ and 4 orders of magnitude, respectively. Given that this calculation uses our upper limit on the estimated Lyman continuum ionizing flux, and therefore

represents a best case scenario for this hypothesis, we are able to rule out thermal expansion of an H II region as the possible driving source of the arc.

### 4.2.2 A wind-blown bubble

The analysis presented in the previous section indicates that there must be a significant source of energy on top of that provided by the thermal pressure of photoionized gas. One possibility is that this energy is provided by the stellar wind. In the following, we explore the possibility that the arc represents the dense, partial shell that surrounds a bubble driven by a stellar wind from a high-mass star. The time evolution of radial expansion of a bubble driven by stellar winds can be expressed (Weaver et al. 1977),

$$R_{\mathrm{W}}(t) = \alpha \left( \frac{L_{\mathrm{wind}}}{\rho_0} \right)^{1/5} t^{3/5}, \tag{21}$$

where $\alpha = [125/154(\pi)]^{1/5}$ (Tielens 2005; Lancaster et al. 2021a), $L_{\mathrm{wind}}$ is the mechanical wind luminosity, $L_{\mathrm{wind}} = 0.5\dot{M}v_\infty^2$, and $\rho_0$ is the ambient density (estimated in Section 4.1).

The Weaver et al. (1977) solution assumes that the wind gas is adiabatic and trapped, so it applies to a bubble that is completely closed and has no cooling. As soon as gas breaks out, or there is significant mixing between hot and cold gas that leads to cooling, the rate of expansion will drop below the Weaver et al. (1977) solution (McKee, van Buren & Lazareff 1984; Mac Low & McCray 1988; Lancaster et al. 2021a). Mac Low & McCray (1988) relaxed the condition that the wind gas is adiabiatic and included radiative cooling from the interior of the bubble. At early times, the expansion follows the analytical Weaver et al. (1977) solution. At later times, some of the internal energy is radiated away and the expansion rate slows. The numerical solution of Mac Low & McCray (1988) grows at a rate close to $t^{1/2}$, such that we can write

$$R_{\mathrm{W_c}}(t) = R_{\mathrm{cool}} \left( \frac{t}{t_{\mathrm{cool}}} \right)^{1/2}, \tag{22}$$

where $R_{\mathrm{cool}} = R_{\mathrm{W}}$, given by equation (21), is the radius of the bubble at a time $t = t_{\mathrm{cool}}$, where $t_{\mathrm{cool}}$ is the time at which radiative cooling becomes significant. Using this expression, we can estimate the time it would take for a wind-blown bubble to expand its current size assuming this time is $> t_{\mathrm{cool}}$:

$$t_{\mathrm{W_c}} = \left( \frac{R_{\mathrm{W_c}}}{\alpha} \right)^2 \left( \frac{L_{\mathrm{wind}}}{\rho_0} \right)^{-2/5} t_{\mathrm{cool}}^{-1/5}. \tag{23}$$

The corresponding expansion velocity, momentum in the shell, and kinetic energy of the shell are

$$v_{\mathrm{W_c}} = \frac{1}{2}\alpha \left( \frac{L_{\mathrm{wind}}}{\rho_0} \right)^{1/5} t_{\mathrm{W_c}}^{-1/2} t_{\mathrm{cool}}^{1/10}, \tag{24}$$

$$p_{\mathrm{W_c}} = M_{\mathrm{arc}} v_{\mathrm{W_c}} = \frac{2\pi}{3}\alpha^4 \left( L_{\mathrm{wind}}^4 \rho_0 t_{\mathrm{cool}}^2 \right)^{1/5} t_{\mathrm{W_c}}, \tag{25}$$

and

$$E_{\mathrm{W_c}} = \frac{1}{2}M_{\mathrm{arc}} v_{\mathrm{W_c}}^2 = \frac{125}{462} L_{\mathrm{wind}} t_{\mathrm{W_c}}^{1/2} t_{\mathrm{cool}}^{1/2}, \tag{26}$$

respectively.

The cooling time can be expressed (Mac Low & McCray 1988; Chevance et al. 2022)

$$t_{\mathrm{cool}} \approx 3000 \left( \frac{Z}{Z_\odot} \right)^{-35/22} \left( \frac{L_{\mathrm{wind}}}{10^{35}\,\mathrm{erg\,s^{-1}}} \right)^{3/11} \left( \frac{n_{\mathrm{H}}}{10^4\,\mathrm{cm^{-3}}} \right)^{-8/11}\,\mathrm{yr}, \tag{27}$$

where $Z$ is the metallicity. To estimate the cooling time, we must therefore estimate the mechanical wind luminosity. As discussed in Section 4.1, both observations (Mokiem et al. 2007) and simulations (Offner & Arce 2015) show that the mass-loss rates from early-type B stars predicted from the models of wind launching considered here (Vink et al. 2001) can be underestimated by orders of magnitude. In the following, we therefore use the mass-loss rates and terminal wind velocities derived for O stars of spectral type O9.5, O9, O8.5 in Section 4.1, under the assumption that these provide the limiting case for this scenario. We therefore estimate the range in mechanical wind luminosity that spans this parameter space, finding $L_{\mathrm{wind}} = 0.4 - 2.2 \times 10^{35}\,\mathrm{erg\,s^{-1}}$ (note that in some cases empirically derived mechanical wind luminosities from early type B stars can actually exceed this range; Mokiem et al. 2007). Inserting numerical values we derive a range of cooling times $t_{\mathrm{cool}} = 1500$–$2200\,\mathrm{yr}$, where the lower limit is given by our lower limit on the mechanical wind luminosity and the upper limit on the cloud density at solar metallicity (the upper limit is given by the opposite at twice solar metallicity). Due to the considerable ambient density of G0.253+0.016, the corresponding cooling time is much shorter than that inferred under the typical conditions found in galaxy discs (Mac Low & McCray 1988; Chevance et al. 2022). Using equation (21), the corresponding size of the wind blown bubble at time $t = t_{\mathrm{cool}}$ is therefore $R_{\mathrm{cool}} = 0.05$–$0.12\,\mathrm{pc}$.

In the top panel of Fig. 6, we show curves corresponding to the time evolution of wind-blown bubbles that represent the extremes of the parameter space described above (orange dashed lines). The model in which the shell swept up by the wind-blown bubble expands most quickly (slowly) is derived from our upper (lower) limits on the stellar mass and metallicity, but the lower (upper) limit on density. The corresponding evolution in the expansion velocity is shown in the bottom panel. Equating $R_{\mathrm{W_c}} = R_{\mathrm{arc}}$, for $M/M_\odot = 19.82$, $\dot{M}(Z/Z_\odot = 2)$, and $n_{\mathrm{H}} \sim 0.4 \times 10^4\,\mathrm{cm^{-3}}$, we derive an age of $t_{\mathrm{W_c}} = 0.4 \times 10^6\,\mathrm{yr}$, an expansion velocity of $v_{\mathrm{W_c}} = 1.5\,\mathrm{km\,s^{-1}}$, a momentum $p_{\mathrm{W_c}} = 0.2 \times 10^4\,M_\odot\,\mathrm{km\,s^{-1}}$, and an energy $E_{\mathrm{W_c}} = 0.6 \times 10^{47}\,\mathrm{erg}$. The same calculation for $M/M_\odot = 16.46$, $\dot{M}(Z/Z_\odot = 1)$, and $n_{\mathrm{H}} \sim 1.9 \times 10^4\,\mathrm{cm^{-3}}$ yields $t_{\mathrm{W_c}} = 1.6 \times 10^6\,\mathrm{yr}$, $v_{\mathrm{W_c}} = 0.4\,\mathrm{km\,s^{-1}}$, $p_{\mathrm{W_c}} = 0.2 \times 10^4\,M_\odot\,\mathrm{km\,s^{-1}}$, and $E_{\mathrm{W_c}} = 0.2 \times 10^{47}\,\mathrm{erg}$.

For the $M = 16.46\,M_\odot$ star, the expansion velocity and momentum are an order of magnitude below the values estimated from the observations, but the predicted energy is lower by $>2$ orders of magnitude. In the case of the $M = 19.82\,M_\odot$ star, the predicted momentum and energy are comparable to within a factor of $<2$ to the measured values, while the predicted expansion velocity is lower by a factor of $\sim 3.5$ compared to our fiducial estimate of $5.2\,\mathrm{km\,s^{-1}}$.[6] While the agreement remains imperfect, this analysis demonstrates that the arc could plausibly represent a dense, partial shell surrounding a bubble driven by a stellar wind. The factor of $\sim$a few discrepancy may be explained by the fact that each of the discussions above consider a single feedback mechanism acting in isolation when in reality different mechanisms may act in concert (Draine 2011b; Yeh et al. 2013; Martínez-González, Silich & Tenorio-Tagle 2014; Mackey et al. 2015). A full prescription of the different feedback mechanisms is beyond the scope of this study and will require detailed modelling tailored to the conditions found in G0.253+0.016 and, more generally, the extreme environment of the CMZ.

---

[6]Note that for the $M = 16.46\,M_\odot$ star, we compare our predicted values to our measured upper limit on density and momentum (worst case scenario) and for the $M = 19.82\,M_\odot$ star the reverse (best case scenario).

### 4.3 Is a wind-blown bubble the most likely scenario?

The analysis presented in the previous sections leads us to conclude the following:

(i) the arc is plausibly the result of stellar feedback.

(ii) the estimated density and morphology of the arc are difficult to reconcile with a scenario in which the arc is a bow-shock swept up by the wind of an interloper star.

(iii) the thermal pressure of photoionized gas alone is unable to reproduce the estimated dynamics and energetics of the arc.

(iv) the arc may represent a dense, partial shell surrounding a bubble driven by the wind from a high-mass star.

The importance of winds from high-mass stars as a feedback mechanism is under recently revived debate. Numerical simulations have had a consensus for some time that generally photoionization dominates over winds (Dale et al. 2013; Geen et al. 2021; Rathjen et al. 2021). Despite this, there are several sources with morphology and dynamics which appear to be consistent with those expected for wind-blown bubbles. RCW 120 has been recently described as being a wind-blown bubble driven by a O8V star moving relative to the ambient cloud material by $<4\,\mathrm{km\,s^{-1}}$, with further evidence to suggest that star formation may have been triggered within the swept-up shell (Luisi et al. 2021). Similarly, Pabst et al. (2019, 2020) recently concluded that the bubble of the Orion Nebula is predominantly driven by the mechanical energy input of the strong stellar wind from the O7V star $\theta^1$ Orionis C (see also Güdel et al. 2008), based on the simple analytical model of Weaver et al. (1977).

This latter interpretation however, faces many challenges. As described in Section 4.2.2, the Weaver et al. (1977) solution assumes that the wind gas is adiabatic and trapped. As soon as the gas cools, the expansion speed will drop below the Weaver et al. (1977) solution. The recent work of Lancaster et al. (2021a, b) demonstrates that turbulence-driven inhomogeneity in the structure of the material surrounding the wind-driven bubbles may strongly affect the impact of the mechanical energy of the wind. The cooling induced by turbulent mixing in the absence of magnetic fields leads to order of magnitude differences in the expansion velocity and imparted momentum compared to those derived in the classical Weaver et al. (1977) solution, although there is evidence that magnetic fields at least partly mitigate this effect (e.g. Gentry et al. 2019). Indeed, the recent numerical simulations of Rosen et al. (2021) also show that wind bubbles blown by individual high-mass stars do not experience efficient mixing in the presence of magnetic fields (Pillai et al. 2015, estimate a total magnetic field strength of $5.4 \pm 0.5\,\mathrm{mG}$ in G0.253+0.016). The magnetic field provides a confining and stabilizing effect and suppresses the development of instabilities that otherwise lead to effective mixing and cooling (Lancaster et al. 2021a, b). It is also worth noting that direct measurements of the X-ray luminosities of wind-blown bubbles are inconsistent with the Weaver et al. (1977) model, and require substantial loss of energy via either turbulent mixing or bulk escape of hot material (Harper-Clark & Murray 2009; Rosen et al. 2014). It may therefore simply be the case that the high velocity C II emission observed by Pabst et al. (2019, 2020) is tracing material from a wind that is escaping along low-density channels in the bubble, rather than driving feedback globally in the region (Haid et al. 2018).

In the Galactic Centre, a number of molecular shell candidates have been identified (Martín-Pintado et al. 1999; Oka et al. 2001; Butterfield et al. 2018; Tsujimoto et al. 2018, 2021). The kinetic energy estimated for many of these shells has led to speculation that they are the result of (potentially multiple) supernova explosions

(e.g. Tsujimoto et al. 2018). However, those identified in Sgr B2 by Martín-Pintado et al. (1999) share many of the properties displayed by the arc in G0.253+0.016. Martín-Pintado et al. (1999) identify a series of $\sim$1–2 pc shells and arcs detected in emission from the (3,3) and (4,4) lines of $NH_3$. (Recall that the arc in G0.253+0.016 is also prominent in these lines – Mills et al. 2015.) They conclude that the shells are expanding with velocities 6–10 $\mathrm{km\,s^{-1}}$ and have an associated kinetic energy of the order $10^{48}$ erg, very similar to the quantities derived for the arc in G0.253+0.016 and considerably smaller than typical energies of $\sim$$10^{51}$ erg associated with supernova-driven shells. The authors speculate that the shells in Sgr B2 are produced by the wind-blown bubbles generated by high-mass stars and describe how the shocks generated by the expansion heat the surrounding gas, further arguing that the expanding shells may have even triggered further star formation within Sgr B2's envelope.

The arc located in G0.253+0.016 provides an interesting new addition to this puzzle. First, the associated radio continuum emission is extended, unlike the compact H II regions driven by O-type stars in other clouds in the Galactic Centre (e.g. Sgr A A-D and H; Goss et al. 1985; Zhao et al. 1993; Mills et al. 2011; Hankins et al. 2019). One possible explanation for this may be because the source driving the arc is less embedded, having formed at the edge of the cloud and excavated a cavity. Second, the morphology, dynamics, and energetics of the arc show reasonable (to within a factor of a few) agreement with a modified form of the Weaver et al. (1977) solution that accounts for cooling within the bubble interior (Mac Low & McCray 1988), but differs from that in Orion (Pabst et al. 2019, 2020) in that it is identified using a molecular (rather than ionized gas) tracer. It is certainly possible that local environmental conditions in the Galactic Centre may help winds to play an important role. In high-density environments, winds may stay contained within the shell longer leading to more prolonged expansion (Barnes et al. 2020). Hence we are left with three possibilities: (i) winds are not the key feedback driving mechanism and some other explanation is required to explain the origin of the arc; (ii) winds are more important for driving feedback than otherwise expected, in such a way that simulations, and the interpretation of observations of winds (e.g. in X-rays) are incorrect; and (iii) winds are less important under normal conditions, but may be more important under the extreme conditions (e.g. high-density, high-metallicity, strong magnetic fields) in the Galactic Centre (e.g. Martín-Pintado et al. 1999; Barnes et al. 2020).

### 4.4 Has G0.253+0.016 already formed a star cluster?

In this section, we address the elephant in the room, namely that if the arc is the result of a wind-blown bubble generated by a high-mass star, then *where is the star?* The short $\sim$760–7000 yr recombination time estimated in Section 3.4 implies that the source of the ionizing radiation must still reside within the cavity enclosed by the arc. If the star has formed *in situ*, as implied by the wind-blown bubble scenario, then the immediate implication is that G0.253+0.016 is perhaps not as quiescent as is commonly accepted. High-mass stars rarely (if at all) form in isolation (de Wit et al. 2004, 2005). Though isolated high-mass stars have been identified throughout the Galactic Centre (Mauerhan et al. 2010; Dong et al. 2011; Clark et al. 2021), the cluster formation efficiency in CMZ clouds may be as high as $\sim$ 30–40 per cent (Ginsburg & Kruijssen 2018).

Assuming the high-mass star forms as part of a star cluster, we can estimate the mass of the parent cluster and address the question of whether or not we would be likely to detect such a cluster towards G0.253+0.016. Again here, we consider only the O star scenario, since this presents the best case scenario for detectability. To estimate
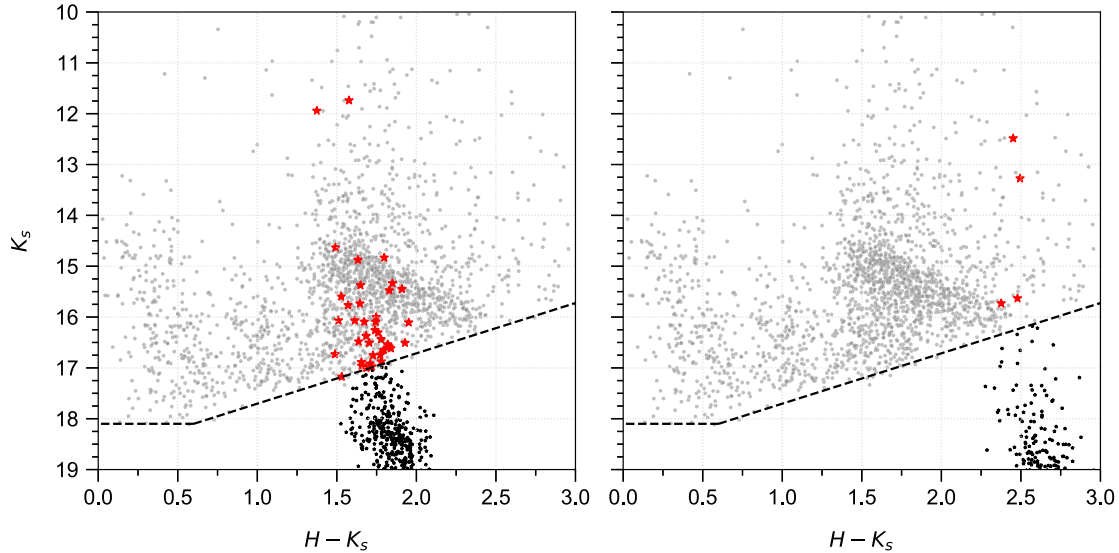
**Figure 7.** CMD $K_s$ versus $H - K_s$ corresponding to the region containing G0.253+0.016 (see fig. 2 in Nogueras-Lara et al. 2021a). Grey dots represent real stars from the GNS survey (Nogueras-Lara et al. 2018, 2019). The red and black stars correspond to the synthetic stellar population of a young (0.5 Myr) cluster of mass 500 M$_\odot$. The red and black stars denote detections and non-detections from the synthetic population, respectively, considering the detection limit of the data (black dashed line). The left-hand and right-hand panels assume an extinction of $A_{K_s} = 2$ and 3 mag, respectively, with the latter indicating fewer detections of cluster members.

the mass of the parent star cluster, we simulate samples of star clusters for a range of cluster masses, generating $n = 10\,000$ clusters of each mass, assuming a standard stellar IMF (Kroupa 2001). For each cluster we determine the mass of its highest mass star, comparing the peak of the distribution to the 16–20 M$_\odot$ relevant for stars of spectral type consistent with our upper limit of the Lyman continuum ionizing flux, $N_{LyC}$ (Martins et al. 2005). We find that cluster masses of the order 400–700 M$_\odot$ are typical for those in which the most massive star is $\sim$16–20 M$_\odot$.

As an independent estimate of the potential cluster mass, we follow the method outlined in Barnes et al. (2017). To do this, we first estimate the bolometric luminosity from infrared luminosity maps of the CMZ using *Spitzer* and *Herschel* observations. Barnes et al. (2017) assume that all the emission from the embedded stellar population within a molecular cloud is reprocessed by the surrounding dust and re-emitted. Under this assumption, the total infrared luminosity directly corresponds to the bolometric luminosity produced by the embedded population. We apply this method to the arc by estimating the total bolometric luminosity within the region defined in Fig. 3, for which we find $L_{bol} \sim 1.2 \times 10^5$ L$_\odot$. We can convert this bolometric luminosity to a stellar mass by assuming that the highest mass star within the cluster dominates the luminosity. To do this, we use the bolometric luminosity-to-mass conversions presented by Davies et al. (2011). For $L_{bol} \sim 1.2 \times 10^5$ L$_\odot$ we find $M_* \sim 31$ M$_\odot$. Repeating the same experiment as before, we find that a cluster mass of the order $\sim$1000 M$_\odot$ is typical for those in which the most massive star is $\sim$31 M$_\odot$. Given the uncertainty in equating the total infrared luminosity to bolometric luminosity, this should be interpreted as a strict upper limit on the total mass of the embedded stellar population (see Barnes et al. 2017 for further details). Although the absolute values should be taken with caution, this analysis suggests that the independent measures of radio continuum emission and the total infrared luminosity are consistent with the presence of a (moderately) high-mass star.

To address whether we would be expected to detect such a star cluster in currently available data, we use the GALACTICNUCLEUS

(GNS) catalogue. The GNS is a high-angular resolution ($\sim$0″.2) *JHK$_s$* survey of the Galactic Centre (Nogueras-Lara et al. 2018, 2019), that partially covers G0.253+0.016. We build a synthetic young cluster with a total mass of 500 M$_\odot$, using PARSEC evolutionary tracks (Bressan et al. 2012; Chen et al. 2014, 2015; Tang et al. 2014; Marigo et al. 2017; Pastorelli et al. 2019, 2020) to obtain $H$ and $K_s$ photometry. We assume twice solar metallicity (Feldmeier-Krause et al. 2017; Schultheis et al. 2019, 2021) and a standard IMF (Kroupa 2001) and create five different models with different ages (0.5, 0.7, 1, and 5 Myr). To redden the data, we test three different scenarios using average extinctions $A_{K_s} = 2$, 2.5, and 3.0 mag. We redden the synthetic data randomly, choosing the extinction value for each star from a Gaussian distribution centred on the average extinctions with a typical standard deviation of $\sim$0.1 mag (Nogueras-Lara et al. 2020). We randomly simulate the photometric uncertainties for each star assuming a Gaussian distribution for each band, with a standard deviation of 0.05 mag corresponding to the expected uncertainty for the GNS data (Nogueras-Lara, Schödel & Neumayer 2021b). Finally, we place the stellar population at the Galactic Centre distance using a distance modulus of 14.52 (Nogueras-Lara et al. 2021a).

We plot the simulated stellar populations on the colour–magnitude diagram (CMD) $K_s$ versus $H - K_s$ towards G0.253+0.016 (Fig. 7; Nogueras-Lara et al. 2021a). Using the limitations of the real GNS data, we identify which of the cluster stars may be detected. Assuming the lowest extinction ($A_{K_s} = 2.0$ mag), $\lesssim$40 stars can be detected for each of the different ages tested and this decreases with increasing cluster age. The most favourable case, in terms of detection, is the youngest cluster age considered (0.5 Myr; Fig. 7). Given the stellar background in the CMD, the differential reddening, and the very low number of potentially observed stars belonging to the young cluster, we conclude that a direct detection using the CMD would be unlikely. Moreover, the assumed extinction of $A_{K_s} = 2.0$ mag corresponds to the value obtained by Nogueras-Lara et al. (2021a) using red clump stars (e.g. Girardi 2016) for the region containing G0.253+0.016. This is the best case scenario for detection and is equivalent to the cluster being situated in the foreground of

the cloud. Assuming a larger extinction of $A_{K_s} = 3.0\,\text{mag}$, we obtain even fewer detections of the cluster members (Fig. 7).

Finally, we also check whether the cluster could be detected due to stellar overdensities in the near-infrared (NIR) images. We use the $K_s$ band, where the extinction is lowest, and compute the stellar density using the GNS data corresponding G0.253+0.016. We divide the observed region into small subregions of $1\,\text{pc}^2$ to compute the number of stars detected in $K_s$. Averaging over all the subregions, we find a mean stellar surface density of $\sim 180 \pm 90\,\text{pc}^{-2}$, where the uncertainty corresponds to the standard deviation of the measurement. Considering the most favourable case of a cluster stellar population of 0.5 Myr, an extinction of $A_{K_s} = 2.5\,\text{mag}$, and assuming that the cluster extends to a radius of $\sim 0.5\,\text{pc}$ (comparable to the Arches, Hosek et al. 2015), the expected overdensity is $\sim 80\,\text{pc}^{-2}$ indicating that the cluster would not easily be detected by its stellar density.

In summary, we conclude that the high extinction and stellar crowding towards G0.253+0.016 is more than capable of hampering the detection of a $500\,\text{M}_\odot$ star cluster in currently available NIR data. Moreover, we stress that the above assumes best case scenario for detection. To detect such a cluster, longer integration time NIR observations would be needed to detect fainter cluster members. However, this may not help if the cluster were deeply embedded within the cloud or behind the main column. The discussions presented in Section 4.3 and here clearly call for further observations to resolve any ambiguity that remains surrounding the possible origins of the arc. Future high-sensitivity observations with other facilities, such as the James Webb Space Telescope (*JWST*), will likely reveal the true star formation activity of G0.253+0.016.

### 4.5 What is the implied star formation rate?

Barnes et al. (2017) provide an upper limit of the total stellar mass of newly formed stars within the Brick of $> 2000\,\text{M}_\odot$ from a measurement of the total infrared emission. These authors estimate a star formation rate of $< 0.007\,\text{M}_\odot\,\text{yr}^{-1}$ based on this total stellar mass and a star formation time-scale based on inferences about the orbit of the cloud ($t_{\text{SF}} = 0.3\,\text{Myr}$). Kauffmann et al. (2017), on the other hand, estimate an upper limit of $\sim 800\,\text{M}_\odot$ based on the absence of any radio or maser emission sources. These authors used a time-scale based on a statistical approach based on the number of observed H II region and masers within the CMZ ($t_{\text{SF}} = 1.1\,\text{Myr}$), and determined a star formation rate of $< 0.0008\,\text{M}_\odot\,\text{yr}^{-1}$. Based on the observed bounds of our derived $N_{\text{LyC}}$ values, we estimate here the associated star formation rate of a $12$–$20\,\text{M}_\odot$ star (section 3.4), under the assumption that this implies the presence of a $\sim 500\,\text{M}_\odot$ cluster (given a standard Kroupa 2001 IMF). Assuming that the cluster has an age $t_{\text{SF}} = 0.4$–$1.6\,\text{Myr}$ (see Section 4.2.2), the associated star formation rate is in the range $0.0003$–$0.0013\,\text{M}_\odot\,\text{yr}^{-1}$. The star formation rates are highly dependent on the assumed time-scales over which they are inferred. None the less, our estimates based on the presence of a single B1-O8.5 star are broadly consistent with the low star formation rates measured within the literature.

## 5 SUMMARY AND CONCLUSIONS

In this paper, we have built on the analysis presented in Henshaw et al. (2019), combining ALMA and VLA observations to determine the origin of the arcuate structure identified within G0.253+0.016. We find evidence for an expanding bubble associated with ionized gas emission. Our main conclusions are summarized below.

Using the kinematic decomposition presented in Henshaw et al. (2019), we find that morphology of the arc can be described

using a simple tilted ring model. The ring is centred on $\{l, b\} = \{0°.248, 0°.018\}$ and has a radius of $R_{\text{arc}} = 1.3\,\text{pc}$. The azimuthal velocity pattern observed along the crest of the arc is broadly consistent with that expected for an expanding incomplete shell. Using our model geometry, we derive an expansion velocity of $v_{\text{exp}} = 5.2^{+2.7}_{-1.9}\,\text{km\,s}^{-1}$. From this information, we infer that the dynamical age of the arc is $t_{\text{dyn}} \approx 2.4^{+0.8}_{-1.4} \times 10^5\,\text{yr}$ (assuming a constant expansion velocity). Using dust continuum observations, we determine the mass off the arc to be $M_{\text{arc}} \sim 2700^{+3000}_{-1400}\,\text{M}_\odot$. Combining with the derived expansion velocity, we measure the kinetic energy and momentum of the arc to be $E_{\text{arc}} \sim 0.7^{+2.8}_{-0.6} \times 10^{48}\,\text{erg}$ and $p_{\text{arc}} \sim 1.4^{+3.1}_{-1.0} \times 10^4\,\text{M}_\odot\,\text{km\,s}^{-1}$, respectively.

Our new radio continuum and RRL data reveal that ionized gas fills the arc cavity. The RRL spectrum extracted from the arc cavity peaks at a velocity of $22.0 \pm 1.4\,\text{km\,s}^{-1}$, consistent to within one standard deviation of the mean of the arc centroid velocity distribution ($17.6 \pm 4.5\,\text{km\,s}^{-1}$). The spatial and kinematic agreement between the ionized and molecular gas emission leads us to conclude that the two are likely physically related. To give insight into the type of source required to stimulate this emission, we calculate the Lyman-continuum photon rate, $N_{\text{LyC}} = 10^{46.0}$–$10^{47.9}\,\text{photons\,s}^{-1}$. The implied short recombination time of $t_{\text{rec}} = 760$–$7000\,\text{yr}$ further suggests that the source of the ionized gas must still be located within the arc cavity. Assuming that the emission is produced by a single zero-age main-sequence star, the estimated $N_{\text{LyC}}$ is consistent with that expected for a high-mass star of spectral type B1-O8.5, corresponding to a mass of $\approx 12$–$20\,\text{M}_\odot$.

We go on to explore the possible origins of the arc and the potential star driving its expansion. We consider two scenarios: (i) the arc represents a shell swept up by the wind of an interloper high-mass star and (ii) the arc represents a shell swept up by stellar feedback resulting from *in situ* star formation. For the former scenario, the CMZ is unique in our Galaxy in that there is a rich population of 'field' high-mass stars, and we show that the probability that a high-mass star may be passing through G0.253+0.016 at the present time is reasonably high. Nevertheless, we deduce that there does not appear to be a way to reconcile the required ionizing continuum with the current mass and radius estimates of the arc under the assumption that the arc represents a bow-shock produced by a slowly moving high-mass star. This size constraint rules out the Arches and Quintuplet clusters as possible sources of any interloper. Given the information currently available to us, we therefore conclude that the arc is plausibly the result of stellar feedback from *in situ* star formation. We compare the morphological and dynamical properties of the arc, as well as its estimated kinetic energy and momentum to simple analytical models describing the expansion of H II regions, finding that the properties of the arc are consistent to within a factor of a few with those produced by a wind-blown bubble generated by a high-mass stars star.

The immediate implication of this result is that G0.253+0.016 may not be as quiescent as is commonly accepted. Assuming that the high-mass star did not form in isolation, our results could mean that G0.253+0.016 has already produced a $\lesssim 10^3\,\text{M}_\odot$ cluster, containing at least one high-mass star. We demonstrate that the high-extinction and stellar crowding observed towards G0.253+0.016 are more than capable of obscuring such a star cluster from view. Future observations are needed to resolve any residual ambiguity left surrounding the origins of the arc. This is important to establish the true underlying star formation rate of molecular clouds in the CMZ, and to precisely establish the role of stellar feedback in shaping the ISM and regulating the star formation process in an environment which has the highest number of high-mass stars per unit volume in

the Galaxy. We suggest that future observations from facilities such as ALMA (to better constrain the mass of the arc) and *the* JWST (to reveal the internal stellar population) will have the sensitivity necessary to confirm or reject this result.

## DATA AVAILABILITY

The data underlying this article will be shared on reasonable request to the corresponding author.

## REFERENCES

Armentrout W. P., Anderson L. D., Balser D. S., Bania T. M., Dame T. M., Wenger T. V., 2017, ApJ, 841, 121

Armillotta L., Krumholz M. R., Di Teodoro E. M., McClure-Griffiths N. M., 2019, MNRAS, 490, 4401

Arthur S. J., Hoare M. G., 2006, ApJS, 165, 283

Bally J. et al., 2010, ApJ, 721, 137

Bally J. et al., 2014, ApJ, 795, 28

Baranov V. B., Krasnobaev K. V., Kulikovskii A. G., 1971, Sov. Phys. Dokl., 15, 791

Barnes A. T., Longmore S. N., Battersby C., Bally J., Kruijssen J. M. D., Henshaw J. D., Walker D. L., 2017, MNRAS, 469, 2263

Barnes A. T., Longmore S. N., Dale J. E., Krumholz M. R., Kruijssen J. M. D., Bigiel F., 2020, MNRAS, 498, 4906

Battersby C. et al., 2011, A&A, 535, A128

Battersby C. et al., 2020, ApJS, 249, 35

Bressan A., Marigo P., Girardi L., Salasnich B., Dal Cero C., Rubele S., Nanni A., 2012, MNRAS, 427, 127

Butterfield N., Lang C. C., Morris M., Mills E. A. C., Ott J., 2018, ApJ, 852, 11

Callanan D. et al., 2021, MNRAS, 505, 4310

Chen Y., Girardi L., Bressan A., Marigo P., Barbieri M., Kong X., 2014, MNRAS, 444, 2525

Chen Y., Bressan A., Girardi L., Marigo P., 2015, IAU General Assembly. p. 2257534

Chevance M. et al., 2022, MNRAS, 509, 272

Clark P. C., Glover S. C. O., Ragan S. E., Shetty R., Klessen R. S., 2013, ApJ, 768, L34

Clark J. S., Patrick L. R., Najarro F., Evans C. J., Lohr M., 2021, A&A, 649, A43

Clarkson W. I., Ghez A. M., Morris M. R., Lu J. R., Stolte A., McCrady N., Do T., Yelda S., 2012, ApJ, 751, 132

Crowther P. A., 2007, ARA&A, 45, 177

Dale J. E., Ngoumou J., Ercolano B., Bonnell I. A., 2013, MNRAS, 436, 3430

Davies B., Hoare M. G., Lumsden S. L., Hosokawa T., Oudmaijer R. D., Urquhart J. S., Mottram J. C., Stead J., 2011, MNRAS, 416, 972

de Wit W. J., Testi L., Palla F., Vanzi L., Zinnecker H., 2004, A&A, 425, 937

de Wit W. J., Testi L., Palla F., Zinnecker H., 2005, A&A, 437, 247

Deharveng L., Peña M., Caplan J., Costero R., 2000, MNRAS, 311, 329

Dong H. et al., 2011, MNRAS, 417, 114

Draine B. T., 2011a, Physics of the Interstellar and Intergalactic Medium, Princeton University Press, Princeton, US

Draine B. T., 2011b, ApJ, 732, 100

Federrath C. et al., 2016, ApJ, 832, 143

Feldmeier-Krause A., Kerzendorf W., Neumayer N., Schödel R., Nogueras-Lara F., Do T., de Zeeuw P. T., Kuntschner H., 2017, MNRAS, 464, 194

Figer D. F., Kim S. S., Morris M., Serabyn E., Rich R. M., McLean I. S., 1999, ApJ, 525, 750

Foster J. B. et al., 2011, ApJS, 197, 25

Geen S., Bieri R., Rosdahl J., de Koter A., 2021, MNRAS, 501, 1352

Gentry E. S., Krumholz M. R., Madau P., Lupi A., 2019, MNRAS, 483, 3647

Giannetti A. et al., 2017, A&A, 606, L12

Ginsburg A., Kruijssen J. M. D., 2018, ApJ, 864, L17

Ginsburg A., Bressert E., Bally J., Battersby C., 2012, ApJ, 758, L29

Ginsburg A. et al., 2016, A&A, 586, A50

Ginsburg A. et al., 2018, ApJ, 853, 171

Girardi L., 2016, ARA&A, 54, 95

Goss W. M., Schwarz U. J., van Gorkom J. H., Ekers R. D., 1985, MNRAS, 215, 69P

Gravity Collaboration, 2019, A&A, 625, L10

Green S., Mackey J., Haworth T. J., Gvaramadze V. V., Duffy P., 2019, A&A, 625, A4

Güdel M., Briggs K. R., Montmerle T., Audard M., Rebull L., Skinner S. L., 2008, Science, 319, 309

Habe A., Ohta K., 1992, PASJ, 44, 203

Habibi M., Stolte A., Harfst S., 2014, A&A, 566, A6

Haid S., Walch S., Seifried D., Wünsch R., Dinnbier F., Naab T., 2018, MNRAS, 478, 4799

Hankins M. J., Lau R. M., Mills E. A. C., Morris M. R., Herter T. L., 2019, ApJ, 877, 22

Harper-Clark E., Murray N., 2009, ApJ, 693, 1696

Hatchfield H. P. et al., 2020, ApJS, 251, 14

Haworth T. J. et al., 2015, MNRAS, 450, 10

Henshaw J. D. et al., 2016a, MNRAS, 457, 2675

Henshaw J. D., Longmore S. N., Kruijssen J. M. D., 2016b, MNRAS, 463, L122

Henshaw J. D. et al., 2019, MNRAS, 485, 2457

Henshaw J. D. et al., 2020, Nat. Astron., 4, 1064

Higuchi A. E., Chibueze J. O., Habe A., Takahira K., Takano S., 2014, AJ, 147, 141

Hosek Matthew W. J., Lu J. R., Anderson J., Ghez A. M., Morris M. R., Clarkson W. I., 2015, ApJ, 813, 27

Hosokawa T., Inutsuka S.-I., 2006, ApJ, 646, 240

Hurley J. R., Pols O. R., Tout C. A., 2000, MNRAS, 315, 543

Immer K., Menten K. M., Schuller F., Lis D. C., 2012, A&A, 548, A120

Jackson J. M. et al., 2013, Publ. Astron. Soc. Aust., 30, e057

Jeffreson S. M. R., Kruijssen J. M. D., Krumholz M. R., Longmore S. N., 2018, MNRAS, 478, 3380

Johnston K. G., Beuther H., Linz H., Schmiedeke A., Ragan S. E., Henning T., 2014, A&A, 568, A56

Kassim N. E., Frail D. A., 1996, MNRAS, 283, L51

Kauffmann J., Pillai T., Zhang Q., 2013, ApJ, 765, L35

Kauffmann J., Pillai T., Zhang Q., Menten K. M., Goldsmith P. F., Lu X., Guzmán A. E., 2017, A&A, 603, A89

Krieger N. et al., 2017, ApJ, 850, 77

Kroupa P., 2001, MNRAS, 322, 231

Kruijssen J. M. D., Longmore S. N., Elmegreen B. G., Murray N., Bally J., Testi L., Kennicutt R. C., 2014, MNRAS, 440, 3370

Kruijssen J. M. D., Dale J. E., Longmore S. N., 2015, MNRAS, 447, 1059

Kruijssen J. M. D. et al., 2019, MNRAS, 484, 5734

Krumholz M. R., 2017, Star Formation. World Scientific Series in Astrophysics. World Scientific Publishing, Singapore

Krumholz M. R., Matzner C. D., 2009, ApJ, 703, 1352

Krumholz M. R. et al., 2014, in Beuther H., Klessen R. S., Dullemond C. P., Henning T., eds, Protostars and Planets VI. University of Arizona Press, Tucson, p. 243

Krumholz M. R., Kruijssen J. M. D., Crocker R. M., 2017, MNRAS, 466, 1213

Lancaster L., Ostriker E. C., Kim J.-G., Kim C.-G., 2021a, ApJ, 914, 89

Lancaster L., Ostriker E. C., Kim J.-G., Kim C.-G., 2021b, ApJ, 914, 90

Lang C. C., Goss W. M., Wood O. S., 1997, ApJ, 474, 275

LaRosa T. N., Kassim N. E., Lazio T. J. W., Hyman S. D., 2000, AJ, 119, 207

Law C. J., Backer D., Yusef-Zadeh F., Maddalena R., 2009, ApJ, 695, 1070

Lindner R. R. et al., 2015, AJ, 149, 138

Lis D. C., Carlstrom J. E., 1994, ApJ, 424, 189

Lis D. C., Menten K. M., 1998, ApJ, 507, 794

Lis D. C., Menten K. M., Serabyn E., Zylka R., 1994, ApJ, 423, L39

Lis D. C., Serabyn E., Zylka R., Li Y., 2001, ApJ, 550, 761

Longmore S. N. et al., 2012, ApJ, 746, 117

Longmore S. N. et al., 2013a, MNRAS, 429, 987

Longmore S. N. et al., 2013b, MNRAS, 433, L15

Longmore S. N. et al., 2014, in Beuther H., Klessen R. S., Dullemond C. P., Henning T., eds, Protostars and Planets VI. University of Arizona Press, Tucson, p. 291

López-Calderón C., Bronfman L., Nyman L.-Å., Garay G., de Gregorio-Monsalvo I., Bergman P., 2016, A&A, 595, A88

Lu X. et al., 2019a, ApJS, 244, 35

Lu X. et al., 2019b, ApJ, 872, 171

Luisi M. et al., 2021, Sci. Adv., 7, eabe9511

McKee C. F., van Buren D., Lazareff B., 1984, ApJ, 278, L115

McLeod A. F., Dale J. E., Evans C. J., Ginsburg A., Kruijssen J. M. D., Pellegrini E. W., Ramsay S. K., Testi L., 2019, MNRAS, 486, 5263

Mac Low M.-M., McCray R., 1988, ApJ, 324, 776

Mac Low M.-M., van Buren D., Wood D. O. S., Churchwell E., 1991, ApJ, 369, 395

Mackey J., Gvaramadze V. V., Mohamed S., Langer N., 2015, A&A, 573, A10

Marigo P. et al., 2017, ApJ, 835, 77

Marsh K. A., Ragan S. E., Whitworth A. P., Clark P. C., 2016, MNRAS, 461, L16

Martín-Pintado J., Gaume R. A., Rodríguez-Fernández N., de Vicente P., Wilson T. L., 1999, ApJ, 519, 667

Martínez-González S., Silich S., Tenorio-Tagle G., 2014, ApJ, 785, 164

Martins F., Schaerer D., Hillier D. J., 2005, A&A, 436, 1049

Martins F., Hillier D. J., Paumard T., Eisenhauer F., Ott T., Genzel R., 2008, A&A, 478, 219

Mauerhan J. C., Muno M. P., Morris M. R., Stolovy S. R., Cotera A., 2010, ApJ, 710, 706

Mehringer D. M., Menten K. M., 1997, ApJ, 474, 346

Menten K. M., 1991, in Haschick A. D., Ho P. T. P., eds, ASP Conf. Ser. Vol. 16, Atoms, Ions and Molecules: New Results in Spectral Line Astrophysics. Astron. Soc. Pac., San Francisco, p. 119

Mezger P. G., Henderson A. P., 1967, ApJ, 147, 471

Mezger P. G., Pankonin V., Schmid-Burgk J., Thum C., Wink J., 1979, A&A, 80, L3

Mills E., Morris M. R., Lang C. C., Dong H., Wang Q. D., Cotera A., Stolovy S. R., 2011, ApJ, 735, 84

Mills E. A. C., Butterfield N., Ludovici D. A., Lang C. C., Ott J., Morris M. R., Schmitz S., 2015, ApJ, 805, 72

Mills E. A. C., Ginsburg A., Immer K., Barnes J. M., Wiesenfeld L., Faure A., Morris M. R., Requena-Torres M. A., 2018, ApJ, 868, 7

Mokiem M. R. et al., 2007, A&A, 473, 603

Molinari S. et al., 2011, ApJ, 735, L33

Morris M., Yusef-Zadeh F., 1989, ApJ, 343, 703

Muijres L. E., Vink J. S., de Koter A., Müller P. E., Langer N., 2012, A&A, 537, A37

Najarro F., Figer D. F., Hillier D. J., Kudritzki R. P., 2004, ApJ, 611, L105

Newville M., Stensitzki T., Allen D. B., Ingargiola A., 2014, LMFIT: Non-Linear Least-Square Minimization and Curve-Fitting for Python, Zenodo

Nogueras-Lara F. et al., 2018, A&A, 610, A83

Nogueras-Lara F. et al., 2019, A&A, 631, A20

Nogueras-Lara F., Schödel R., Neumayer N., Gallego-Cano E., Shahzamanian B., Gallego-Calvente A. T., Najarro F., 2020, A&A, 641, A141

Nogueras-Lara F., Schödel R., Neumayer N., Schultheis M., 2021a, A&A, 647, L6

Nogueras-Lara F., Schödel R., Neumayer N., 2021b, A&A, 653, A33

Offner S. S. R., Arce H. G., 2015, ApJ, 811, 146

Oka T., Hasegawa T., Sato F., Tsuboi M., Miyazaki A., 2001, PASJ, 53, 787

Ossenkopf V., Henning T., 1994, A&A, 291, 943

Pabst C. et al., 2019, Nature, 565, 618

Pabst C. H. M. et al., 2020, A&A, 639, A2

Panagia N., 1973, AJ, 78, 929

Pastorelli G. et al., 2019, MNRAS, 485, 5666

Pastorelli G. et al., 2020, MNRAS, 498, 3283

Petkova M. A. et al., 2021, preprint (arXiv:2104.09558)

Pillai T., Kauffmann J., Tan J. C., Goldsmith P. F., Carey S. J., Menten K. M., 2015, ApJ, 799, 74

Ponti G. et al., 2015, MNRAS, 453, 172

Portegies Zwart S. F., McMillan S. L. W., Gieles M., 2010, ARA&A, 48, 431

Rathborne J. M. et al., 2014a, ApJ, 786, 140

Rathborne J. M. et al., 2014b, ApJ, 795, L25

Rathborne J. M. et al., 2015, ApJ, 802, 125

Rathjen T.-E. et al., 2021, MNRAS, 504, 1039

Riener M., Kainulainen J., Henshaw J. D., Orkisz J. H., Murray C. E., Beuther H., 2019, A&A, 628, A78

Rodríguez L. F., Zapata L. A., 2013, ApJ, 767, L13

Rosen A. L., Lopez L. A., Krumholz M. R., Ramirez-Ruiz E., 2014, MNRAS, 442, 2701

Rosen A. L., Offner S. S. R., Foley M. J., Lopez L. A., 2021, preprint (arXiv:2107.12397)

Rubin R. H., 1968, ApJ, 154, 391

Schultheis M., Rich R. M., Origlia L., Ryde N., Nandakumar G., Thorsbro B., Neumayer N., 2019, A&A, 627, A152

Schultheis M. et al., 2021, A&A, 650, A191

Simpson J. P., Colgan S. W. J., Cotera A. S., Kaufman M. J., Stolovy S. R., 2018, ApJ, 867, L13

Simpson J. P., Colgan S. W. J., Cotera A. S., Kaufman M. J., Stolovy S. R., 2021, ApJ, 910, 59

Smith N., 2014, ARA&A, 52, 487

Smith L. J., Norris R. P. F., Crowther P. A., 2002, MNRAS, 337, 1309

Sormani M. C., Tress R. G., Glover S. C. O., Klessen R. S., Battersby C. D., Clark P. C., Hatchfield H. P., Smith R. J., 2020, MNRAS, 497, 5024

Spitzer L., 1978, Physical Processes in the Interstellar Medium. A Wiley-Interscience Publication, New York

Storey P. J., Hummer D. G., 1995, MNRAS, 272, 41

Takahira K., Tasker E. J., Habe A., 2014, ApJ, 792, 63

Tang J., Bressan A., Rosenfield P., Slemer A., Marigo P., Girardi L., Bianchi L., 2014, MNRAS, 445, 4287

Tang Y., Wang Q. D., Wilson G. W., 2021, MNRAS, 505, 2377

Tielens A. G. G. M., 2005, The Physics and Chemistry of the Interstellar Medium. Cambridge University Press, Cambridge, UK

Tress R. G., Sormani M. C., Glover S. C. O., Klessen R. S., Battersby C. D., Clark P. C., Hatchfield H. P., Smith R. J., 2020, MNRAS, 499, 4455

Tsujimoto S., Oka T., Takekawa S., Yamada M., Tokuyama S., Iwata Y., Roll J. A., 2018, ApJ, 856, 91

Tsujimoto S. et al., 2021, ApJ, 910, 61

Urquhart J. S. et al., 2018, MNRAS, 473, 1059

Vink J. S., de Koter A., Lamers H. J. G. L. M., 2001, A&A, 369, 574

Walker D. L., Longmore S. N., Bastian N., Kruijssen J. M. D., Rathborne J. M., Jackson J. M., Foster J. B., Contreras Y., 2015, MNRAS, 449, 715

Walker D. L. et al., 2021, MNRAS, 503, 77

Weaver R., McCray R., Castor J., Shapiro P., Moore R., 1977, ApJ, 218, 377

Wilson T. L., Rohlfs K., Hüttemeister S., 2009, Tools of Radio Astronomy. Springer, Berlin, Heidelberg

Yeh S. C. C., Verdolini S., Krumholz M. R., Matzner C. D., Tielens A. G. G. M., 2013, ApJ, 769, 11

Yusef-Zadeh F., 1989, in Morris M., ed., Vol. 136, The Center of the Galaxy. Kluwer Academic Publishers, Dordrecht, p. 243

Zhao J.-H., Desai K., Goss W. M., Yusef-Zadeh F., 1993, ApJ, 418, 235

This paper has been typeset from a TEX/LATEX file prepared by the author.